Master Thesis

Faculty of Science
University of Bern

Tracking Heatwaves in the Northern Hemisphere

Handed in by Nicolas Hartmann

Supervisor: Prof. Dr. Olivia Romppainen-Martius
Advisors: Duncan Pappert & Dr. Edgar Dolores-Tesillos

June 2024

Oeschger Centre for Climate Change Research,
University of Bern

Abstract

Heatwaves pose a significant threat to society, including impacts on human health, agriculture, and wildfires. Due to anthropogenic climate change, these impacts are anticipated to worsen in the future. To better understand the characteristics of such impactful events, this thesis examines heatwaves in the Northern Hemisphere using a Lagrangian feature-tracking algorithm, ConTrack which was originally developed to identify atmospheric blocking. In this thesis, heatwaves are tracked between 1959 to 2023 using the ERA5 reanalysis dataset. The analysis addresses the following questions: Can ConTrack track temperature anomalies? What regions experience the most heatwaves? What is the typical duration and size of heatwaves in the Northern Hemisphere? Does El Niño impact the size of heatwaves ? By analyzing the recent intense heatwave in 2021 in the Pacific Northwest, it was shown that ConTrack can identify temperature anomalies. Subsequently, it was found that the frequency maxima are linked with atmospheric blocking in the Pacific Northwest and North of Europe, and persistent high pressure systems in the Pacific and Atlantic. The average size value of heatwaves ranges from 1 to almost 20 $[10^6 \times \text{km}^2]$ with the smallest occurring over land (in North America, north of Europe, Central Sahara, Arabia, and Siberia) and the largest over central Pacific, the Caribbean Sea, and east of Atlantic. The median duration varies from 3 to 12 days with the shortest heatwaves occurring over North America, Siberia, and Southeast Asia. In contrast, the longest heatwaves occur in Central America, in the Atlantic and Pacific Ocean. Generally, the longest heatwaves are also among the largest ones. Lastly, this thesis shows that the size of heatwaves is smaller in the Pacific Northwest, and larger in South Asia, Eastern Europe, and western North America during El Niño conditions.

Contents

1 Introduction

Heatwaves, often defined as prolonged periods of excess heat (Perkins and Alexander [2013]; Perkins [2015]), pose a significant threat to society. They can lead to severe impacts on impacts human health (e.g., Thompson et al. [2018]; Vicedo-Cabrera et al. [2021]), agriculture (e.g., Brás et al. [2021]; Chakraborty et al. [2019]; Fraga et al. [2020]), wildfires (e.g., Borchers Arriagada et al. [2020]; Hegedűs et al. [2024]; Parente et al. [2018]; Westerling et al. [2006]), infrastructure (e.g., Ke et al. [2016]; Darryn McEvoy and Mullett [2012]), labor productivity and the economy (e.g., García-León et al. [2021]; Orlov et al. [2019]; Xia et al. [2018]). For example, with solely the European heatwave in 2003 about 70,000 thousand excess deaths were recorded (Fouillet et al. [2006]; Robine et al. [2008]). Over the past decades, the duration, frequency, intensity, and spatial extent of heatwaves have increased (Perkins and Alexander [2013];Perkins-Kirkpatrick and Lewis [2020]). The latter has been well studied in North America (Keellings et al. [2018]; Lyon et al. [2019]). For example, Rogers et al. [2022] explored characteristics of large concurrent heatwaves on a larger scale encompassing the entire Northern Hemisphere. All these studies found an increase in heatwave frequency and severity in the past few decades. In the future, these metrics are expected to further rise as the climate warms in response to increasing greenhouse gas concentrations (Hoegh-Guldberg et al. [2018]; Meehl and Tebaldi [2004]; Seneviratne et al. [2021]).

Heatwaves can be studied at varying spatial and temporal scales and temperature thresholds. For instance, some studies focus on single events (e.g., Philip et al. [2021]; Schär et al. [2004]), and others on heatwaves affecting a specific region (e.g., Böhnisch et al. [2023]; Dong et al. [2013]; Stéfanon et al. [2012]). In addition, some studies have looked at favorable conditions influencing heatwave propagation and severity such as sea surface temperature (SST) (e.g., Beobide-Arsuaga et al. [2023]; Feudale and Shukla [2010]), soil moisture (e.g., Lorenz et al. [2010]; Zampieri et al. [2009]) and associated weather patterns (e.g., Chan et al. [2022]; Grotjahn et al. [2015]; Pfahl [2014]; Tuel et al. [2022]). For instance, atmospheric blocking can significantly influence near-surface temperatures. According to the definition based on the works of Berggren et al. [1949] and Rex [1950] as given in Steinfled and Pfahl [2019], blocking is described as: "the formation of persistent, quasi-stationary, large-scale anticyclonic circulation anomalies that disrupt or block the prevailing westerly flow." This phenomenon shields the affected region from storms, resulting in clear skies that create favorable conditions for temperatures to rise due to changes in circulation and radiative forcing. Moreover, other researchers have examined the properties of heatwaves to quantify the processes involved. Extreme temperatures can result from three primary physical processes: the advection of air from climatologically warmer regions to cooler ones, adiabatic compression and subsequent warming in descending air masses, and diabatic heating near Earth's surface through surface sensible heat fluxes, as well as turbulent and convective mixing (Röthlisberger and

Papritz [2023]). For example, Zschenderlein et al. [2019] investigated which processes dominate along heatwave trajectories over Europe. Correspondingly, Röthlisberger and Papritz [2023] identified what processes dominated each region globally.

In terms of the research on the spatial and temporal changes of heatwaves, most studies take an Eulerian, or fixed point of view (e.g., Beobide-Arsuaga et al. [2023]; Perkins-Kirkpatrick and Lewis [2020]). However, only a few studies have investigated the moving patterns of heatwaves from a Lagrangian point of view (Luo et al. [2022, 2024]; Wu et al. [2024]).These studies are limited in their scope to specific regions or land areas. Therefore, a broader assessment of these characteristics, including heatwaves occurring over both land and sea, is still lacking.

In this thesis, I examine heatwaves in the Northern Hemisphere using a Lagrangian feature-tracking algorithm, ConTrack (Steinfeld [2020]) that was originally developed to identify atmospheric blocking. The initial step of the thesis entails determining if ConTrack effectively identifies heatwaves, a task that has not been previously undertaken. This involves addressing the following questions: Is ConTrack capable of tracking temperature anomalies? How does it capture events like the 2021 Pacific Northwest Heatwave? Can analyzing specific regions provide insights into their underlying causes? The second step investigates heatwave characteristics including frequency, duration, and size over the Northern Hemisphere by answering those questions: What regions experience the most heatwaves? What is the typical duration and size of heatwaves in the Northern Hemisphere? The third step delves into assessing the impact of the El Niño–Southern Oscillation (ENSO) on the size of heatwaves, seeking answers to the following questions: Are heatwaves larger during El Niño conditions? La Niña conditions? Do regional differences in heatwave size exist in response to ENSO conditions?

This thesis is structured as follows. In Section 2, the current state of knowledge and the presentation of the tracking algorithm are given. Section 3 presents the data and the methods. In Section 4, the results are shown and discussed. Lastly, the conclusions are drawn in Section 5.

2 Literature Review

2.1 Background and Context

Heatwaves have been extensively studied, and in recent years, even more attention has been drawn to this topic (Marx et al. [2021]). Despite analyzing the same phenomena, comparison of results among studies can be challenging. Although they all agree in words that heatwaves are a prolonged period where temperatures are hotter than normal, the specific definitions, chosen thresholds, and identification methods differ substantially (Perkins [2015]). Here are some examples of studies on heatwaves to illustrate these variations.

Böhnisch et al. [2023] investigated the recurrent pathways of heatwaves. Heatwaves were defined as a minimum of 3 consecutive hot days, separated by at least three non-hot days. A 'hot day' was determined as a day where the maximum surface temperature exceeded the local 95^{th} percentile for June, July, and August (JJA) from the climatology 1981–2010.

The study conducted by Beobide-Arsuaga et al. [2023], investigated the role of SST as a precursor to heatwaves. They defined heatwaves using the maximum surface temperature when it exceeded the 90^{th} percentile, based on a centered 15-day $\times$ 31-year moving average, for at least 3 consecutive days during historical simulations spanning from 1850 to 2005.

Stéfanon et al. [2012] classified heatwave events in the Euro-Mediterranean region into clusters. They also used the maximum surface temperature to set a threshold. An extreme temperature anomaly with respect to the climatology (1950–2009) was defined as exceeding the 95^{th} percentile of the local probability density function calculated using a centered 20-day moving average. Thus, a heatwave had to maintain this exceedance for at least 4 consecutive days. In addition to temperature and temporal thresholds, this study defined a spatial extension requirement, where a grid point must have at least a certain portion of its surface where the temperature exceeds the intensity threshold.

In the Special Report Global Warming of 1.5°C, the IPCC defines a heatwave as a "period of abnormally hot weather" (Hoegh-Guldberg et al. [2018]). They also acknowledge that various interpretations are possible, leading to diverse definitions across studies. As highlighted by the three previous studies, substantial differences exist in the definition of heatwaves, even though all three studies used surface temperature. To detect temperatures "hotter than normal," one can refer to either a reference period (a climatology) or a temperature distribution calculated from a moving window. The main difference between the two is that a reference period retains the trend, while a moving window does not. Therefore, depending on the aim of the study, researchers may choose one method over the other. In addition, the definition of extreme temperatures varies, with thresholds set at either the 90^{th} or 95^{th} percentile, and the minimum duration of heatwaves also varies (3, 4, or 6 days). All these examples demonstrate that while all studies agree on the concept of a heatwave, there is no consensus on the exact

statistical definition. Therefore, there is no right or wrong approach, and each study, with its specificity, highlights different aspects of heatwaves.

So far, only research focusing on heatwaves from an Eulerian perspective (where the focus is on one location in time) has been presented. However, some studies have examined heatwaves from a Lagrangian perspective (where the focus is on the heatwave itself, tracking it in time and space). Within this framework, it becomes possible to analyze the properties of heatwaves along their trajectories. Röthlisberger and Papritz [2023] examined the dominant physical processes (adiabatic, diabatic, and advective) leading to the formation of air masses with extreme temperatures. Similarly, Zschenderlein et al. [2019] assessed which processes had the largest influence on temperature. Bieli et al. [2015] found that extreme hot temperature events were generally associated with weaker horizontal transport from a Lagrangian perspective. This aligns with the previous findings from Pfahl and Wernli [2012], where they also found that high temperatures are often associated with blocking. It is noteworthy that both studies reached similar conclusions despite adopting opposite perspectives. This comparison suggests that both approaches provide valuable insights into heatwaves, offering complementary information.

With ConTrack, I analyzed the properties of heatwaves occurring over contiguous regions, commonly referred to as contiguous heatwaves in the literature (simply referred to as "heatwave" in this thesis). Studies have investigated the spatial extent of contiguous heatwaves over the United States. It has been found that their spatial extent has increased in the past (Keellings et al. [2018]) and is projected to continue expanding in the future (Lyon et al. [2019]). Similar findings have been reported by Vogel et al. [2020]. Additionally, Rogers et al. [2022] tracked large contiguous heatwaves occurring simultaneously in remote regions to assess their relation to different atmospheric patterns. They used daily mean surface temperature during the extended summer season MJJAS (May, June, July, August, September) in the Northern Hemisphere. Heatwaves were defined as periods of at least 3 days with temperatures exceeding the local 90^{th} percentile based on the 1981-2010 climatology. While their study explored intensity and size, it did not investigate spatial frequency or movement patterns.

In contrast, Luo et al. [2022] and Luo et al. [2024] investigated these characteristics for contiguous heatwaves. Initially focusing on China in their 2022 study, they expanded their research globally in their 2024 analysis. They used a three-dimensional (latitude $\times$ longitude $\times$ time) tracking algorithm to identify contiguous heatwaves and their moving patterns. They defined heatwaves as periods when the daily maximum surface temperature exceeded the 95^{th} percentile for a minimum of 3 days, based on a 15-day moving window centered on the same calendar day from 1981 to 2010, covering at least one grid (resolution of $2.5° \times 2.5°$). They established that most heatwaves move eastward and found positive trends in frequency and the total distance traveled by heatwaves, with a negative trend in their average moving speed.

Additionally, they provided average and median values over continents for metrics including size and duration, which will be compared to those obtained in this study. However, their latest study lacked a comprehensive spatial view of the results, including heatwaves occurring over land and sea, which this thesis aimed to address. Moreover, Wu et al. [2024] used very similar methods to track contiguous heatwaves and to observe how ENSO influences the movement properties of these heatwaves. They found that contiguous heatwaves are likely more frequent, more persistent, and have longer travel distances, but move slower during El Niño than La Niña conditions.

In addition, Tamarin-Brodsky et al. [2020] examined regional temperature variability in response to global warming, considering both cold and warm anomalies. They emphasized the importance of considering changes in skewness in the temperature distribution, in addition to those related to variance and shifts in the mean highlighted in Schär et al. [2004]. They used a Lagrangian tracking tool that was typically used for cyclone tracking. While direct comparisons with this thesis are complicated due to differences in research aims and data used, their work showcased the potential for adapting existing tools to explore novel applications.

2.2 Heatwave Tracking Algorithm

The relationship between heatwaves and atmospheric blocking has been well established in previous studies (Chan et al. [2022]; Pfahl and Wernli [2012]; Tuel et al. [2022]). Although these are simplified definitions, both phenomena involve regions experiencing abnormally high temperatures or high pressure for extended periods. Due to this similarity, one could argue that the methods for detecting such events can be relatively similar. Consequently, this study aims to identify heatwaves and analyze their characteristics using a tool called ConTrack (Steinfeld [2020]), which was originally developed to detect atmospheric blocking based on the index from Schwierz et al. [2004]. This allowed us to observe the location, frequency, duration, and size of heatwaves.

However, using ConTrack for heatwave detection comes with several challenges, as the tool was not originally intended for this purpose. To provide some context, it is helpful to review how ConTrack has been utilized in other studies. In several instances, researchers have used a Potential Vorticity (PV) field to detect blocks (e.g., Pfahl and Wernli [2012]; Steinfeld et al. [2020]; Steinfeld et al. [2022]). This method is convenient, as a block can be considered a region where PV exceeds 1.3 PV units (pvu) for typically 4 or 5 days. Additionally, another study used geopotential height over mid to high latitudes to assess the robustness of the PV approach (Steinfled and Pfahl [2019]). Regardless of the variable used, blocks are stationary weather patterns. Therefore, most studies use similar overlap parameters (see Section 3.2) (e.g., Steinfeld et al. [2020]; Tuel and Martius [2024]). However, there are no prescribed parameters for identifying heatwaves. The definition of a heatwave is highly dependent on its

application, and several studies use different ones (Perkins [2015]). Additionally, heatwaves can move rapidly or be more stationary (Luo et al. [2024]). Therefore, using a similar overlap and minimum duration parameters as those used in blocking studies would potentially exclude certain categories of heatwaves. This highlights the difficulty of applying blocking detection methodologies to identify heatwaves. As a consequence, there are no prescribed parameters one can use. For these reasons, a sensitivity test was conducted to observe how ConTrack's output reacted to different sets of parameters and to assess what was most suitable for the analysis. The details are discussed in Appendix A.

3 Data & Methods

3.1 ERA5 Reanalysis Data

The fifth-generation reanalysis data (ERA5) from the European Centre for Medium-Range Weather Forecast (ECMWF) was used. It provides hourly estimates of numerous atmospheric and land-surface parameters on 137 levels from the surface to 0.01 hPa from 1940 to the present with a spatial resolution of $0.25^\circ \times 0.25^\circ$ (Hersbach et al. [2020]). The dataset starts on January 1 1959 and is updated continuously. Thus, ERA5 is a temporally and spatially consistent high-resolution picture of past conditions at each grid point. However, it must be noted that this product is the best guess at the state of the atmosphere currently available but it may differ from reality.

The study area is limited to the Northern Hemisphere and the spatial resolution was upscaled to $0.5^\circ \times 0.5^\circ$. Only data from April to October spanning from 1959 to 2023 for surface temperature (2m temperature (T2m) in ERA5) were used. In addition, the daily mean was calculated using temperature values at 00:00, 06:00, 12:00 and 18:00 (UTC).

3.2 Heatwave Identification

To track heatwaves, ConTrack was applied to a temperature anomaly field obtained by standardizing the daily mean temperature at each grid point. This involved subtracting the mean, estimated over a centered 31-day, 9-year running window, and dividing by the standard deviation for MJJAS between 1959 and 2023, as described in Tuel and Martius [2024]. This procedure effectively removed seasonality and long-term trends, allowing for a focus on the sub-seasonal timescale during which heatwaves develop.

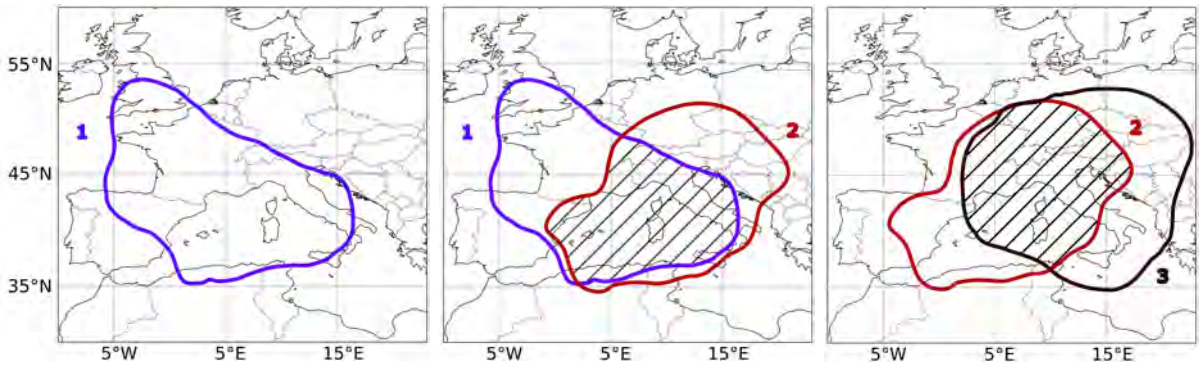

Figure 1: Schematic illustrating a 3-day heatwave. Each panel depicts a temperature anomaly contours surpassing the local 90^{th} percentile. The hatching pattern delineates the 50% contour overlap area, indicating regions where the second (and the third) contour covers at least half of the previous one.

Heatwaves were defined as periods of 3 or more consecutive days with the temperature anomaly exceeding the local 90^{th} percentile, similar to Rogers et al. [2019] and Rogers et al.

[2022]. Then, only heatwaves during JJA, including those beginning in May/August and finishing in June/September (JJA* hereafter), were retained for analysis. Additionally, heatwaves were identified with a 50% contour overlap, meaning that the second contour needed to be covered by at least 50% of the previous one (see Figure 1) where contours are areas above the local 90^{th} percentile. This condition needed to be fulfilled between each time step.

3.3 Heatwave Characteristics

The output of ConTrack gives information about every individual contour of all heatwaves identified. It includes the date, the location (coordinates of the center of the individual contour), and the size. With this data, it is possible to calculate the frequency, the average size, and the median duration of heatwaves at each grid point.

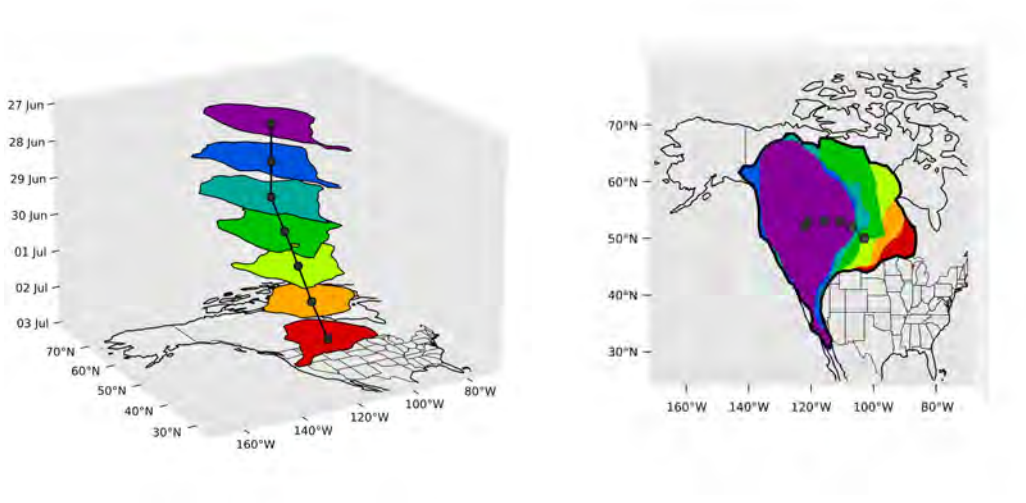

Figure 2: Comparison of the contour types used in the analysis based on the same heatwave: Individual contours depicted on the left, contrasting with the accumulated area contour illustrated on the right.

To observe the spatial distribution of heatwaves over time in the Northern Hemisphere, the heatwave frequency was calculated for each grid point. This calculation involves determining the mean of a binary field, where grid points experiencing a heatwave are assigned the value 1, while those without are assigned 0 over the selected time period. Consequently, the frequency value attributed to a grid point represents the percentage of time during which a heatwave was detected at that specific location during the summer months (JJA*) from 1959 to 2023. The average size was calculated similarly. Instead of assigning the value 1 to the contours, the actual size value of each contour was used in the computation. Both the frequency and the size average considered the individual contours shown in Figure 2 (left). The median duration considered the accumulated area contours (Figure 2, right). The same methodology as before was applied and the duration value was attributed to the accumulated area contour

for every heatwave. Then, it is possible to know the average size and the median duration of heatwaves tracked during the summer months (JJA*) from 1959 to 2023 at any given location in the Northern Hemisphere.

3.4 ENSO: Definition & Identification

El Niño Southern Oscillation (ENSO) is the most important source of interannual variability and is characterized by three phases that occur at irregular intervals. El Niño conditions are referring to the positive (or warm) phase while the negative (or cold) phase is called La Niña. In the tropical Pacific Ocean when neither of these phases are prevailing, the oscillation is said to be neutral. They are represented in Figure 3.

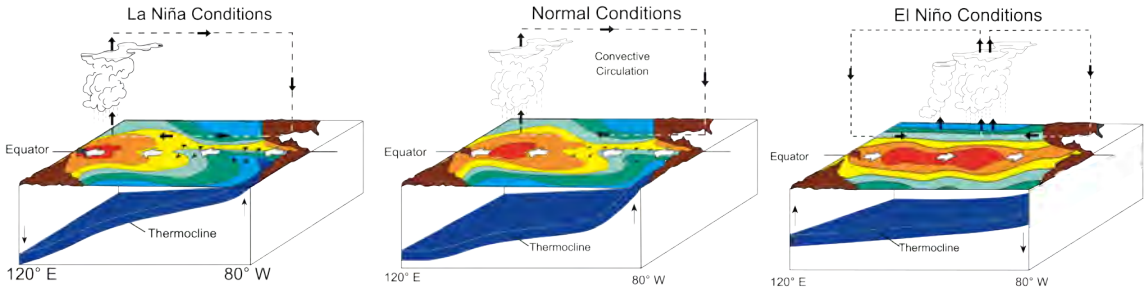

Figure 3: Sketch of the three ENSO phases taken from Stocker et al. [2020].

Under normal conditions, the rising air and the temperature gradient between the western and eastern Pacific maintain strong trade winds. It pushes the warm water to the West causing oceanic upwelling and cooling in the eastern Pacific. If the cooling is strong, then it is said to be a La Niña event. Thus, positive feedbacks maintain the surface branch of the Walker circulation with air rising in the western Pacific and sinking in the eastern Pacific (Stocker et al. [2020]). On the other hand, during El Niño conditions, trade winds weaken, the ocean upwelling is suppressed along the coast of America and the SST rises (Brönnimann [2007]). The temperature gradient prevailing decreases which further weakens the trade winds. As a result, the convective activity is shifted to the central Pacific with a reverse Walker circulation (Brönnimann [2007]).

A common theory to explain the exchange of heat in the tropical Pacific Ocean with other parts of the ocean is based on the delayed oscillator paradigm from Suarez and Schopf [1988]. During La Niña phases the heat builds up in the equatorial Pacific Ocean while it is transported out during El Niño phases. Trenberth et al. [2002] evidenced that most of these exchanges are through diabatic exchanges of heat with the atmosphere including evaporation and thus latent heating in precipitation. The atmospheric circulation changes and differences in cloudiness associated with ENSO result in direct warming, while the release of ocean heat leads to warming that occurs with a delay. These mechanisms drive the teleconnections with

other parts of the world (such as Central America and Southeast Asia) through reduced precipitation and increased solar radiation that contribute to surface warming which peaks several months after the El Niño event (Trenberth et al. [2002]). It has been shown that El Niño conditions seem to impact heatwaves in several regions (Lin et al. [2018]; Luo and Lau [2019]; Pai et al. [2022]; Reddy et al. [2021]) and globally (Wu et al. [2024]).

The ENSO phase can be identified with the Oceanic Niño Index (ONI) from NOAA [2024] as proposed by Chou et al. [2003], Li et al. [2013], and Lin et al. [2018]. Mature El Niño (La Niña) events were identified as such when the boreal winter months (December, January, February) have an ONI seasonal average greater (smaller) than 0.9°C (-0.9°C). Then, an ENSO summer is defined as the months of June, July, and August following the mature phase of ENSO. As a result, 13 La Niña summers (1971, 1974, 1976, 1985, 1989, 1996, 1999, 2000, 2008, 2011, 2018, 2021, and 2022) as well as 12 El Niño summers (1964, 1966, 1969, 1973, 1983, 1987, 1992, 1995, 1998, 2003, 2010, and 2016) were analyzed. Figure 4 displays the number of events per year as well as its ENSO conditions.

I used a composites analysis to explore the link between heatwave size and ENSO conditions. To do so, I calculated the average size of heatwaves during the 12 El Niño summers (13 La Niña summers) minus the total average size.

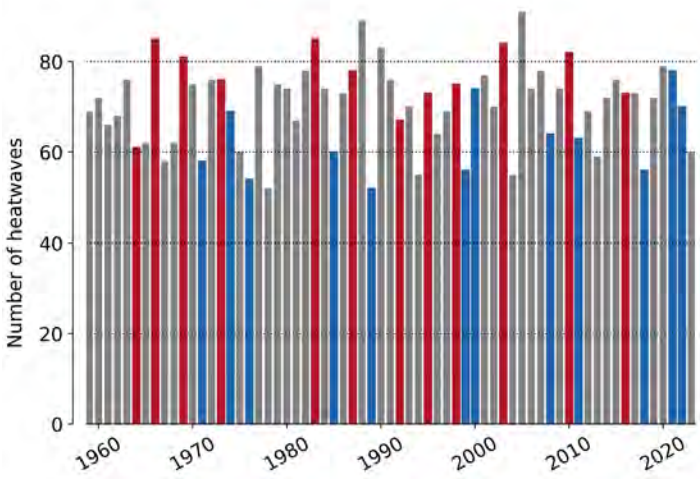

Figure 4: Number of heatwaves per year occurring in the Northern Hemisphere during JJA* from 1959 to 2023. Red bars represent summer with El Niño conditions, blue bars represent summer with La Niña conditions, and grey bars represent summer with neutral ENSO conditions.

3.5 The West Central Sahara region Definition

In the West Central Sahara (WCS) (5°W-5°E; 20°N-30°N), heatwaves exhibit specific characteristics unique to this region. As demonstrated in Section 4.2.1, this area features a high frequency of heatwaves (Figures 4.2.1 and 25) that are generally short (Figure 11) and among

the smallest on average (Figure 12) in the Northern Hemisphere. Due to these distinct traits, I decided to examine the heatwaves detected in this region in greater detail. To do this, I selected events that spent at least one day in WCS (based on the center of individual contours) and excluded events with incoherent tracks.

3.6 Statistical Methods

To visualise and easily compare results (especially size) box plots are used. The box indicates 25% and 75% quartile range, the line within the box is the median, and the whiskers show 5% and 95% range (without outliers).

Additionally, a similar approach to Tuel and Martius [2024] was used to assess the significance of the results in Section 4.3. I used 500 composite maps such as Figure 15 (or Figure 29) were computed from randomly generated selections of years. Each calculation was based on 12 (13 for La Niña) random summers, not based on the specific criteria outlined in Section 3.4. Then, the rank value of each grid point in the ENSO composite was deduced among the 501 iterations (500 random + the ENSO composite). Based on this ranking, an empirical p-value was obtained, and subsequently adjusted for the false discovery rate (Wilks [2016]). Only grid points with an adjusted p-value < 0.1 were considered statistically significant.

4 Results & Discussions

4.1 Case studies

This results section provides insights into ConTrack's performance in tracking heatwaves by examining individual contours from a well-known heatwave. Additionally, it analyzes the characteristics of a specific region in detail. Each case study focuses on a distinct aspect of ConTrack: the individual contours and the tracks, respectively.

4.1.1 The 2021 Pacific Northwest Heatwave

In June 2021, the Pacific Northwest (PNW) experienced an extreme heat event to a magnitude never observed before and several temperature records were broken, including a new all-time Canadian record of 49.6°C in Lytton (Overland [2021]; Philip et al. [2021]; White et al. [2023]). It is considered as one of the most extreme heatwaves since 1960 (Thompson et al. [2022]). Like many heatwaves in the midlatitudes, this event was linked to an unusual behavior of the jet stream (Pfahl and Wernli [2012]; Qian et al. [2022]), known as blocking (Figure 7). A week before the event, a ridge developed over the PNW region which advected warm air from lower latitudes. At the same moment, cyclogenesis occurred along the coast of Alaska induced by a cut-off that traveled from southwest to northeast. As the jet meandered, both features evolved into an "Omega Block" configuration (Woollings et al. [2018]). The mature block can be observed in Figure 7 on 26 June 2021 to 28 June 2021 and it lasted until the 30 June 2021. Until the arrival of the block, the potential temperature within the boundary layer was well-mixed. However, as the upper-level warm core associated with the block arrived, the isentropes moved down and created a very stable warm air column (Neal et al. [2022]). Within these conditions, the surface heat fluxes were dominated by abnormally high solar radiations sinking down and sensible heat flux moving upward that were enhanced by below-average soil moisture (Ansah and Walsh [2021]; Neal et al. [2022]). Additionally, the sinking motion prevented the air column from radiative cooling as well as suppressing convection at the surface. During that period, the geopotential height reached a record high level (Neal et al. [2022]; Philip et al. [2021]) and temperature increased drastically within a few days (Figure 5a). The advected warm air (from the ridge) got trapped within the anticyclone and was further heated. As a result, the intense heat measured at the surface was a "thermodynamic response of the lower troposphere to an anomalously stable stratification aloft set up by the block and heating from below." (Neal et al. [2022])

With the tracking algorithm, ConTrack, I acquired a dataset of heatwaves during the summer months (JJA*) from 1959 to 2023. The PNW heatwave was such a significant event (Philip et al. [2021]) that it is intriguing to analyze how ConTrack has tracked such a well-known heatwave. ConTrack captured the event from 27 June 2021 to 3 July 2021, while

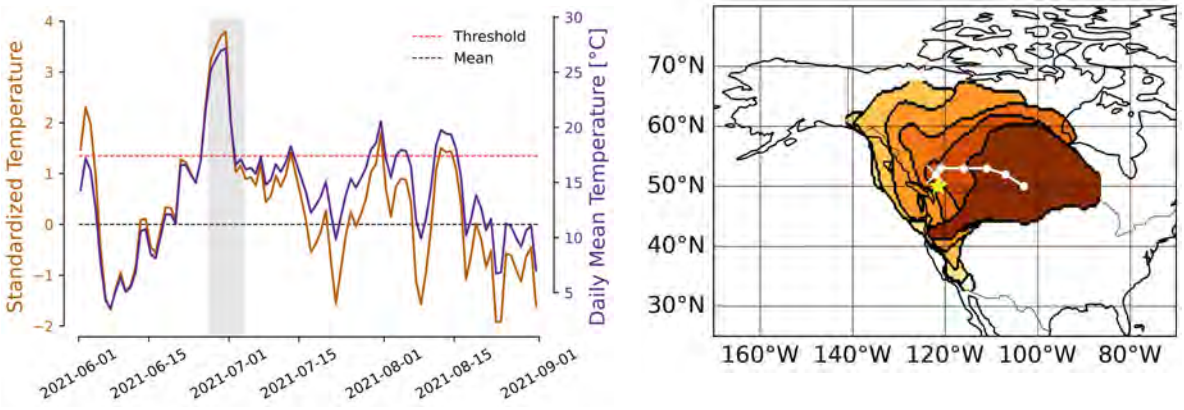

(a) (b)

Figure 5: **a)** Time series of standardized temperature anomaly (in orange shade) and daily mean surface temperature (in purple) during summer 2021 at Lytton (121.5°W, 50.0°N). The horizontal lines represent the local 90^{th} percentile intensity threshold (in red) and the local mean (in black). The grey rectangle shows the period during which individual contours were identified (from 27 June to 03 July 2021).**b)** Spatial extent of the individual contours at each time step from the first day (light shade) to the last one (dark shade). The star shows the location of Lytton. The white dots show the track of the event with the first day marked by a cross.

the temperature and dynamics seemed to already be in place (Figures 5a, 6, and 7). It has been shown that a lag of 2-3 days occurred between the maturation of the block and the temperature peak (Neal et al. [2022]), but this alone cannot explain why the tracking started later. As specified in Section 3.2, a heatwave must meet 3 criteria. The intensity should be above the local 90^{th} percentile, the minimum duration is 3 days, and it needs to meet the 50% overlap criteria between each time step. Referring to Figures 5a and 6, it appears that the intensity criterion was already met before the tracking started around Lytton, while the duration is not an issue as the event lasted 7 days. As a result, after examining the evolution of the temperature anomaly field (Figure 6), it can be observed that the temperature increased rapidly, as did the size of the anomaly. The eventual individual contour prior was probably situated very close to the starting point of the heatwave, but its size was likely smaller. Therefore, the reason why it was not tracked earlier is likely due to the 50% overlap criterion not being met. Due to the rapid temperature increase, the size of the individual contours increased significantly. Therefore, even though the eventual individual contour on the 26^{th} of June 2021 was at the same location, it did not cover 50% of the individual contour on the 27^{th} of June. Conversely, it is likely to be the same reason why the tracking stopped on the 3^{rd} of July and not later. The remaining results presented in Section 4 are obtained from the same heatwave dataset, in which similar occurrences can happen at times. Therefore, it is worth noting that these results are subject to the same biases of this methodology.

In addition to the background atmospheric circulation, Figure 7 shows the individual contours detected for each day. It can be observed that they accurately reflect the shape of the anticyclone of the omega block where the temperature rose. Extreme temperatures are

Date	Center of mass		Size [$10^6 \times km^2$]	Speed [km/day]
	Longitude	Latitude		
27.06.2021	-122	52	3.76	NaN
28.06.2021	-122	52	4.04	0
29.06.2021	-121	53	4.39	130.36
30.06.2021	-116	53	4.54	335.62
01.07.2021	-111	53	3.62	335.62
02.07.2021	-107	52	2.93	293.50
03.07.2021	-103	50	2.90	358.17
Average	-	-	3.74	242.21

Table 1: Characteristics of the 2021 PNW heatwave for each day as identified by ConTrack.

the result of various processes Röthlisberger and Papritz [2023]. ConTrack, in turn, tracks the shape of the temperature signature of these processes. Since the main driver of this exceptional heatwave was the circulation Schumacher et al. [2022], it is not surprising to observe that the individual contours and their characteristics reflect the prevailing blocking conditions. It is important to note that ConTrack can capture such features highlighting its capability in tracking heatwaves.

In this paragraph, I compare the characteristics of the PNW heatwave detected by ConTrack to the other results found in this analysis. The duration of the heatwave (7 days) aligns well with the results from Figure 11. Over the PNW region, it was found that heatwaves lasted between 6 to 8 days over land, where this heatwave developed. However, the PNW heatwave was smaller than the average, as the size of the individual contours varied between 3 to 4.5 $\times$ 10^6 [km^2], while the average is around 6 $\times$ 10^6 [km^2] over this region (Figure 12). It is perhaps not surprising to observe smaller sizes, considering that summer 2021 was marked by La Niña conditions as defined in Section 3.4. The PNW region usually experiences smaller heatwaves during La Niña conditions (Figure 29). During its lifetime, it also showed an average size variation, with size peaking between the first and the last day (Figure 13b).

Additionally, it is worth comparing these characteristics to those found in other studies. The PNW heatwave propagated from West to East as the majority of events typically do in this region (Figure 13 b); Luo et al. [2024]). Moreover, the average speed during this event was 242 [km/day], and it traveled for 1453 [km]. In comparison, the average speed in North America is 297 [km/day] (Luo et al. [2024]) and the average total distance is about 2600 [km]. The below-average speed and total distance can be explained by the prevailing blocking conditions occurring during the heatwave, hindering its movement (Figure 13 a). Additionally, the geopotential height observed during the heatwave was the highest ever recorded at 598 [gpdm] in the region (Philip et al. [2021]). However, compared to the long-term trend of the geopotential height at the 500 [hPa] level in the region, it was not substantially anomalous

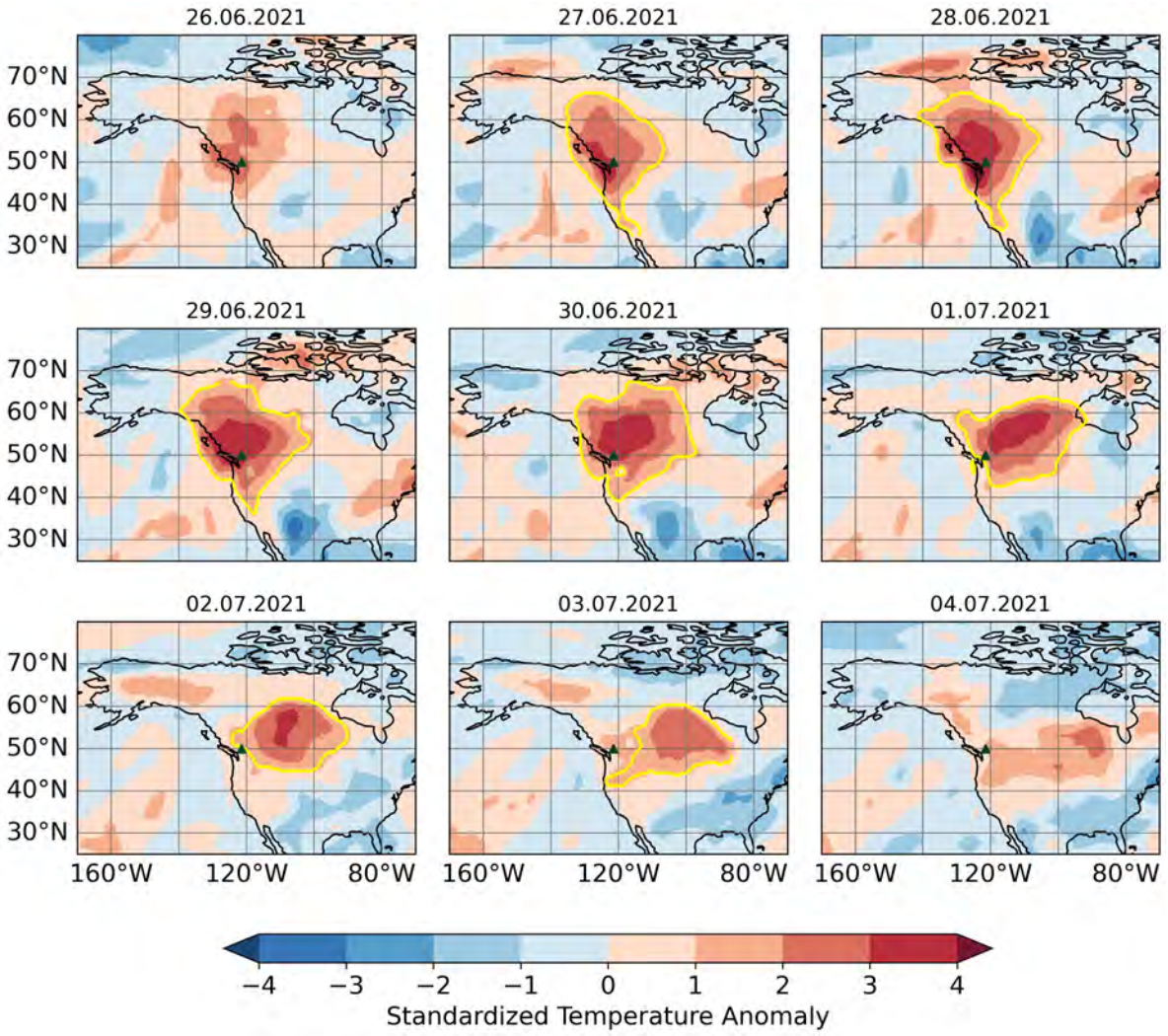

Figure 6: Temperature anomaly field during the 2021 PNW Heatwave, including one day before and after (26 June - 04 July 2021). The seven individual contours identified by ConTrack are depicted in yellow. The location of Lytton (121.5°W, 50.0°N) is indicated by the green triangle.

(Philip et al. [2021]). Thus, what distinguished it from previous heatwaves was its intensity (Figure 5a; McKinnon and Simpson [2022]). There are two theories to explain it: either it was a random event, or non-linear feedback and interactions placed this heatwave in a new category of unknown statistics (Philip et al. [2021]).

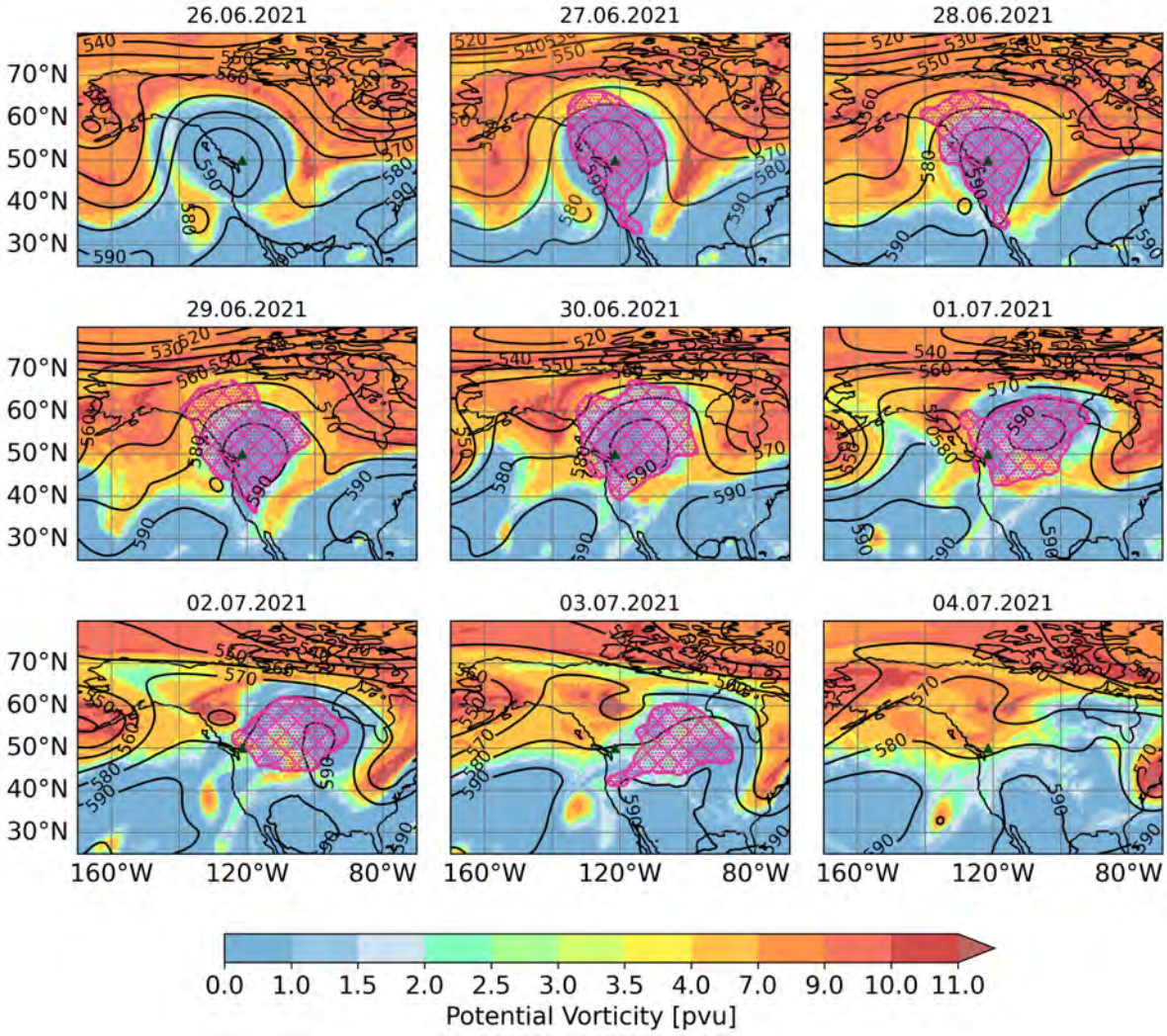

Figure 7: Atmospheric conditions observed during the 2021 PNW Heatwave, including one day before and after (26 June - 04 July 2021). All nine panels show Potential Vorticity [pvu] (shading) along the 340K isentrope, Geopotential Height [gpdm] at the 500 hPa level (black contours), and the seven individual contours identified by ConTrack (pink hatching). Note the non-linear colorbar. The location of Lytton (121.5°W, 50.0°N) is indicated by the green triangle.

4.1.2 The West Central Sahara Region

The West Central Sahara region features a high frequency of heatwaves (Figures 4.2.1 and 25) that are short (Figure 11) and among the smallest on average (Figure 12) in the Northern Hemisphere. For those reasons, I decided to examine the heatwaves detected over this region.

In total, 85 heatwaves were identified, and Table 2 presents the average characteristics values for heatwaves detected over the WCS region. When possible (speed and size), results from all individual contours were also calculated. According to the results, the size of heatwaves over this region is among the smallest in the Northern Hemisphere. They fall on the lower end of the overall size distribution (Figures 12, 13b, and 23 (90^{th} percentile)). Luo et al.

	Frequency [Count]	Median duration [Days]	Avg. speed [km/day]	Avg. Size [$10^5 \times km^2$]	Avg. Tot. distance [km]
Individual Contours	433	-	128.15	5.92	-
Heatwaves	85	4	104.2	4.34	524.68

Table 2: Characteristics of heatwaves that occurred over the WCS region between 1959 and 2023 during JJA*.

[2024] found that the average total distance was about 3340 [km], and the average speed was 424.36 [km/day] for heatwaves over Africa. The averages for the heatwaves described here are well below these values. As it is the case with size (Figure 12) and duration (Figure 11), this region exhibits contrasting characteristics compared to the rest of the African Continent. In addition, the frequency during either El Niño or La Niña (Figure 14) has a similar magnitude over this region. Additionally, compared to other regions, positive or negative ENSO phase revealed little to no effect on heatwave size over this region (Figures 15 and 29). From that, it is fair to assume that ENSO has a limited influence on heatwaves frequency and size in the WCS region. Moreover, 55% of heatwaves are smaller than 2.5 [$10^5 \times km^2$], whereas the largest events (> 10 [$10^5 \times km^2$]) represent only 7%. As observed in Figure 8, the longest heatwaves tend to travel the furthest. In contrast, heatwaves lasting 3 and 4 days tend to be stationary. The longest-living event (light grey in Figure 9) only spent one day in the region. However, long heatwaves do not necessarily always travel long distances, as a 14-days-long one stayed within the region. This characteristic represents the behavior of heatwaves in WCS well as 88% of them spent their entire lifetime without moving out of the region.

Figure 9 illustrates the three heatwaves that traveled the furthest, shaded in grey. The crosses mark the first days, while the center of each individual contour at each time step is represented by dots. Therefore, it is possible to track the propagation of heatwaves. For instance, two of them moved westward, while one moved eastward, aligning with the preferred directions of heatwaves in Africa (Luo et al. [2024]). Then, it is easy to track the trajectory of each event. Rather than plotting 85 tracks, I counted the number of contours that appeared at each location. Consequently, purple dots indicate that between 1 and 10 events occurred at these coordinates, while pink dots highlight the most frequently recurring locations. Thus, pink coordinates represent the most frequently visited locations by heatwaves occurring in the WCS. This indicates that most individual contours were detected at the same location. Additionally, from Figures 26 and 27, it can be observed that both the first and last days occur at the same locations. Consequently, the heatwaves detected over that region are, on average, stationary.

Most heatwaves in the WCS region are characterized by being small, short-lived, and stationary. This reveals a specific category of heatwaves. The location of WCS coincides with the usual location of the Saharan Heat Low during summer (Lavaysse et al. [2009]). A heat low forms as a region of low atmospheric pressure near the surface due to the warming of

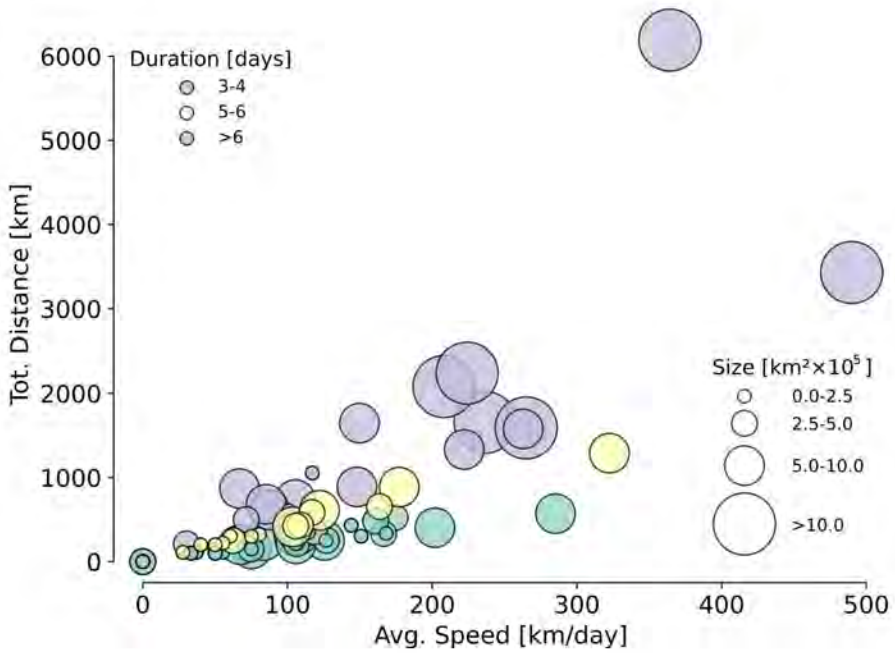

Figure 8: Scatter plot depicting the relationship between total distance traveled [km] and average speed [km/day] for the 85 identified heatwave in the WCS region between 1959 and 2023. Each data point is color-coded based on its duration, and the size of each dot varies according to its size characteristics.

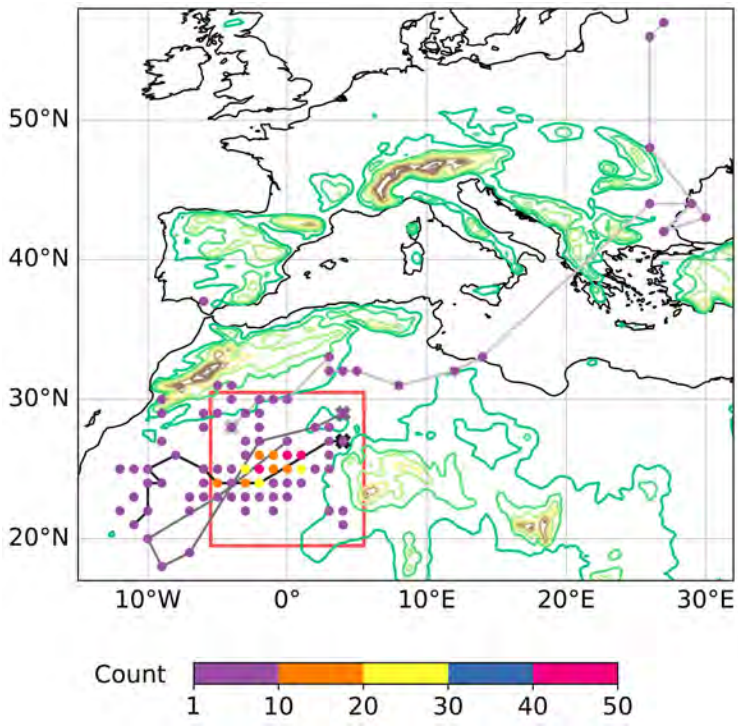

Figure 9: Frequency counts indicating how frequently individual contours (center of the contour) of heatwaves visited a location between 1959 and 2023 during JJA*. The three longest tracks are plotted in grey shading, the genesis location is marked by a cross. The topography within the elevation range of 500 to 1500 meters, with contours every 300 meters, is depicted in green to brown shading. The WCS region is delineated by the red box.

the lower troposphere, leading to the elevation of isobaric surfaces and the divergence of air at higher altitudes (Lavaysse et al. [2009]). Subsequently, the upward motion in the heat low generates an anticyclonic circulation that impacts the structure and dynamics of the African easterly jet. The flat terrain stretching between the Atlas Mountains (to the northwest) and the Hoggar Mountains (to the east) as well as the maximum solar radiation, create favorable conditions for the event to occur repeatedly at the same location (Lavaysse et al. [2009]). Consequently, it is understood to be an important dynamic part of the African Monsoon system (Lavaysse et al. [2009]). The Saharan Heat low is also quasi-stationary during summer (Lavaysse et al. [2009]). Therefore, I believe that most of the identified heatwaves in the WCS region are heat lows, given their characteristics. Therefore, tracking these heatwaves can provide broader insights into African Monsoon dynamics and their impacts. Additionally, a similar assumption can be made for the region showing a high frequency over the Arabian Peninsula (Figure 10), although it has not been specifically analyzed here. This region exhibits similar characteristics and also shows a high frequency of heat lows (Fonseca et al. [2022]).

4.2 Heatwaves Characteristics

4.2.1 Results

Frequency

ConTrack tracks heatwaves based on three parameters, as described in Section 3.2. Consequently, the tracking tool searches for contours that meet these criteria (a minimum of three days, with a 50% overlap) within the 10% warmest temperatures. This is why there are spatial differences evident in Figure 10. The frequency represents the fraction of days a region experienced a heatwave (an individual contour). Thus, a frequency of 5% indicates that the location encountered heatwaves during 5% of the summer days between 1959 and 2023.

The heatwave frequency exhibits a land-sea contrast, with maximum frequencies typically observed over the sea. High frequencies of heatwaves occur notably in the Pacific, between Hawaii and the West Coast of the United States, in the Gulf of Alaska, and the tropical Pacific region. Similarly, the eastern part of the Atlantic Ocean along the coast of Morocco and the Arabian Sea regularly experience heatwaves. Over Europe, there are two frequency maxima: one situated over the Mediterranean and the Black Sea, and the other over Scandinavia.

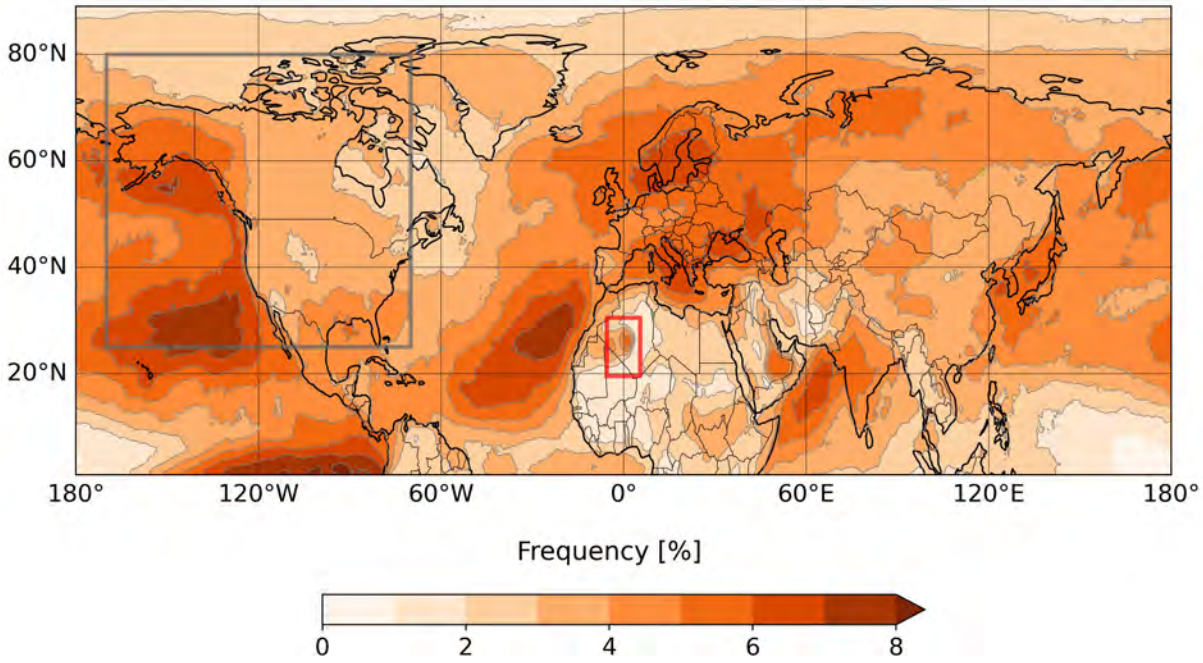

Figure 10: Northern Hemisphere JJA* heatwave (individual contours) frequency from 1959 to 2023. The grey box indicates the Pacific Northwest region discussed in Section 4.1.1, and the red box indicates the West Central Sahara region explored in Section 4.1.2.

Overland, regions including Europe, India, Alaska, the West Central Sahara and the Arabian Peninsula frequently experiences heatwaves. Conversely, the areas experiencing the fewest heatwaves include the Central Pacific, the western region of Africa, the eastern region of Canada, the area between Iran, Afghanistan, and Pakistan, and latitudes above 80°N. Notably, this pattern remains consistent regardless of the temperature threshold selected, as depicted in Figure 24.

Duration

Figure 11 displays the median duration of a heatwave at each grid point for summers between 1959 and 2023, calculated based on the accumulated area contour of each detected heatwave. The duration ranges from a minimum of 3 days up to 12 days. It is important to note that some events lasted longer, as only the median duration is represented. The longest heatwaves occurred over Central America, the Caribbean Sea, and the western tropical Pacific. Extended durations are also observed between Hawaii and the West Coast of the United States, as well as in the Atlantic between Central America and Africa.

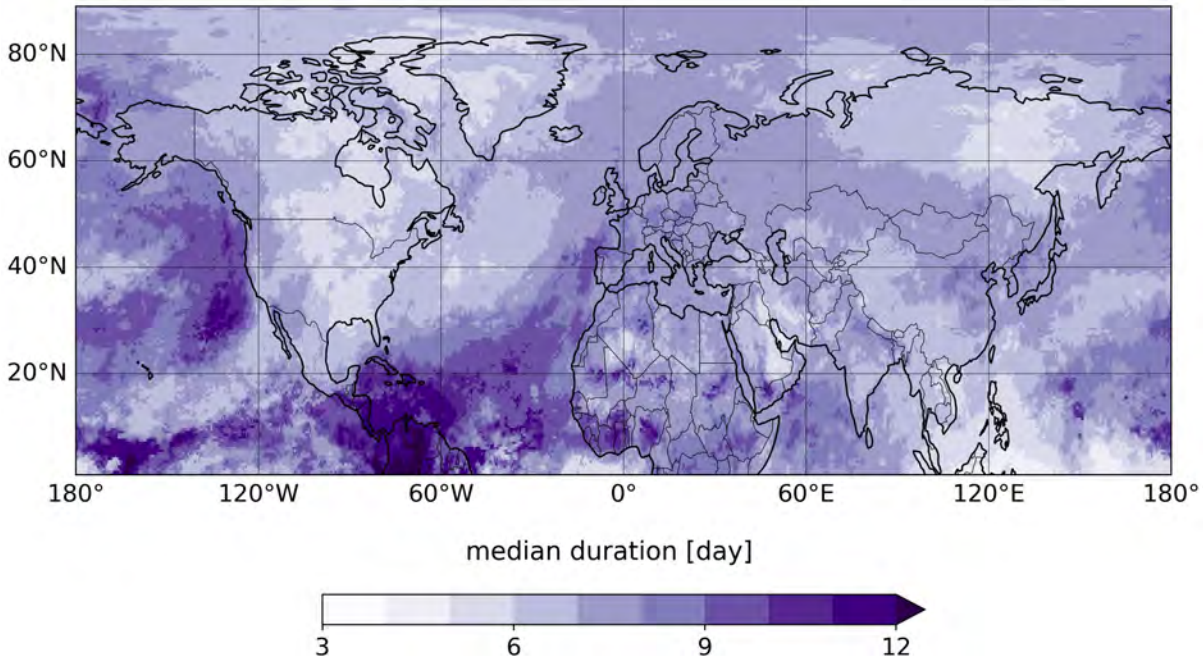

Figure 11: The median duration of heatwaves (accumulated area contour) in the Northern Hemisphere during JJA* from 1959 to 2023.

Conversely, the shortest durations are located over Southeast Asia, northeastern America, Siberia, the western coast of South America, and the Arabian Peninsula, where the median duration ranges from 4 to 5 days. Notably, in North America, heatwaves appear to be shorter compared to those in Europe. It appears that, generally, heatwaves occurring over land are shorter than those over the sea, if Central America is omitted. In Africa, the duration varies from short to long-lasting events and it is relatively unclear to attribute a single value for the median duration over this continent compared to Eurasia and North America. Additionally, more variation in duration is observed between the Equator and the Tropic of Cancer compared to higher latitudes.

Size

Figure 12 illustrates the average size of a heatwave at each grid point for summers between 1959 and 2023, calculated based on the individual contours of each detected heatwave. The range of value spans from 1 to almost 20 [$10^6 \times \text{km}^2$]. This indicates a magnitude difference of almost 20 between regions experiencing the smallest and largest heatwaves.

The largest events occur in the tropical central Pacific, Central America, the Caribbean Sea, and the Atlantic between Central America and Africa. Similarly to the median duration, great sizes are also observed between Hawaii and the West Coast of the United States, as well as in the Atlantic. In contrast, the smallest events are typically over land in regions including the WCS region, the Arabian Peninsula, Siberia, northern Europe, and northern and western Canada. Except for these locations, the size of heatwaves appears to be similar over the

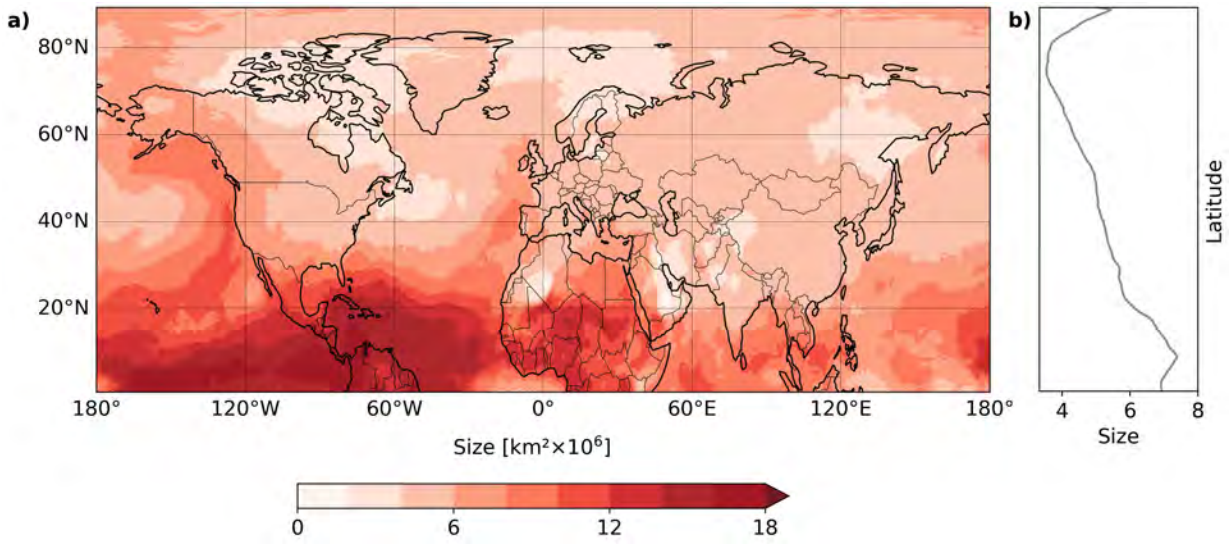

Figure 12: **a)** Average size of heatwaves (individual contours) in the Northern Hemisphere during JJA* from 1959 to 2023. **b)** Mean average size with latitude.

continents, especially over Eurasia and western North America. Over the sea, the smallest heatwaves are located in the regions north of Scandinavia and west of Canada. Additionally, Figure 13b reveals that the size of heatwaves typically varies throughout their lifetime. It displays the size distribution of individual contours on the first (yellow) and last (dark red) day of heatwaves, as well as all the contours in between (grey). This indicates that, based on the criteria defined in Section 3.2, ConTrack is capable of capturing changes in heatwave size during its lifetime as in Vogel et al. [2020]. Additionally, it captures a wide range of heatwave sizes, as it can be observed in Figures 13b and 13a which illustrates the relationship between the duration and the size of heatwaves.

4.2.2 Discussion

Several frequency maxima were identified in Figure 10. Here, I offer hypotheses to explain why these regions experienced a lot of heatwaves. The tropical central Pacific region does resemble the typical El Niño pattern (Scaife et al. [2017]). Additionally, there is a high correlation between SST and surface temperature (Trenberth et al. [2002]), which could explain why a high frequency of heatwaves was observed over that region. In addition, Figure 10 also displays the mean sea level pressure (at the 1020 hPa level) during summers between 1959 and 2023. This illustrates the location of the Azores High over the Atlantic and the North Pacific High along the West coast of the United States (Mokhov et al. [2020]). Similar to the link between blocking and heatwaves, persistent high-pressure systems provide favorable conditions for temperatures to rise. Specifically, the two frequency maxima co-located with these two high-pressure systems are situated away from the storm track (Laurila et al. [2021])

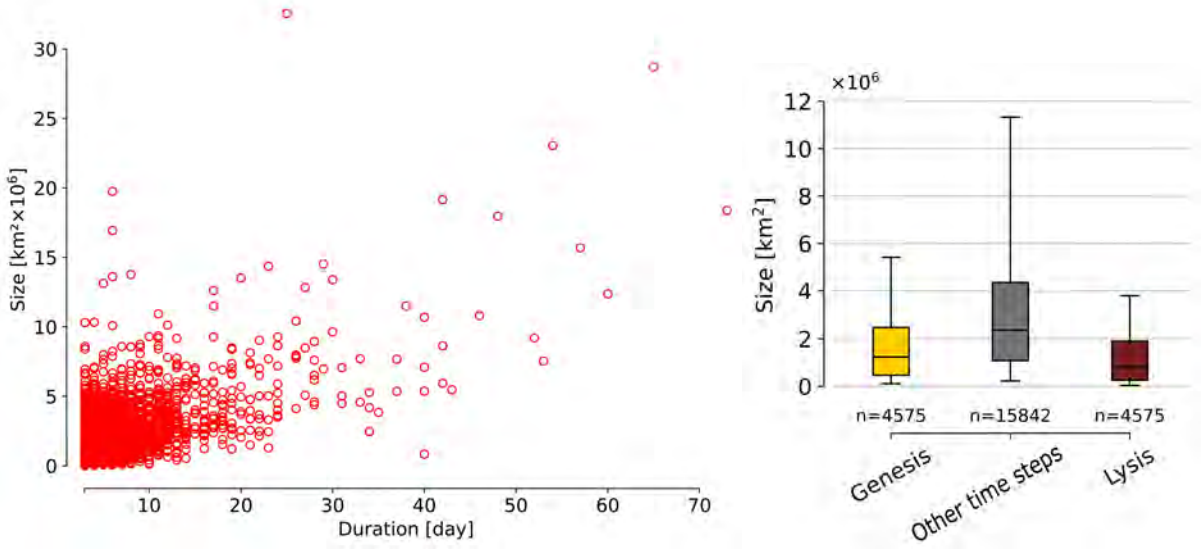

(a) (b)

Figure 13: **a)** Average size plotted against the duration for heatwaves identified in the Northern Hemisphere during JJA* from 1959 to 2023. Each circle represents one heatwave. **b)** Size distribution of heatwave individual contours in the Northern Hemisphere during JJA* from 1959 to 2023. The size distribution of genesis (first day) contours is shown in yellow, lysis (last day) contours in brown, and all other contours except for genesis and lysis in grey.

as well as the hurricane track (Trepanier [2020]). Moreover, the frequency maxima over the Gulf of Alaska and the North of Europe are two regions known to exhibit a high frequency of blocking during the summer (Pfahl and Wernli [2012]). Additionally, the region over the Indian Ocean may be related to the Indian Ocean Dipole (IOD)(Reddy et al. [2021]) and/or ENSO (Brönnimann [2007]). During El Niño conditions, India generally experiences warmer conditions (Kenyon and Hegerl [2008]). This would explain the high frequency observed over those locations. Furthermore, as highlighted in Section 4.1.2, there are strong arguments to link the heatwaves tracked over the WCS region to heat lows, as they are common over this region (Lavaysse et al. [2009]). The same assumption can be made for the frequency maxima in the Arabian Peninsula, as heat lows frequently occur there as well (Fonseca et al. [2022]). In contrast, there are several regions showing frequency minima. It is not particularly surprising to observe a low frequency over the central Pacific. This is because convective activity typically prevails in this area during normal ENSO conditions, as it is where the branches of the Walker circulation ascend (Stocker et al. [2020]). Additionally, in the west of Canada, while this region experiences less blocking compared to the two others mentioned (the Gulf of Alaska and North of Europe), the proportion of extreme temperatures related to blocking is notably higher (Pfahl and Wernli [2012]). Therefore, the frequency of heatwaves is lower as it is likely that ConTrack only captured a few heatwaves related to blocking over that region.

Jiménez-Esteve and Domeisen [2022] have also calculated heatwave frequency based on the temperature at the 850 [hPa] level instead of the 2m temperature. This level is typically above the boundary layer, but it is still highly correlated with the surface (Schneider et al. [2014]; Tamarin-Brodsky et al. [2020]) thus comparison between their results and the ones presented here is possible. Generally, both results agree on the frequency maxima over the Pacific (between Hawaii and the West Coast of the United States and in the Gulf of Alaska), the Atlantic and North of Europe, and on the frequency minima over Central Pacific, Africa, and west of Canada. However, different frequencies are observed over high latitudes and in the typical El Niño regions identified in Figure 10. Additionally, Jiménez-Esteve and Domeisen [2022] have found that topography plays an important role in heatwave frequency by accelerating or slowing the jet stream. This is especially relevant in the Rocky Mountains, where fewer heatwaves tend to occur downstream (to the west) due to the accelerated jet (Jiménez-Esteve and Domeisen [2022]). This would explain the lower frequency found over North America in Figure 10. Moreover, this mountain range seems to influence the characteristics of heatwaves, as the size of heatwaves becomes smaller (Figure 12) and shorter (Figure 11) eastward to the Rocky Mountains.

The calculations for Figure 10 were based on the individual contours (depicted in Figure 2). In this case, a long heatwave will have as many contours as there are time steps, which means that the frequency result in Figure 10 favored long-lasting events over short ones. However, it is also possible to do a similar calculation by counting the heatwave accumulated area contours instead. This is shown in Figure 25. Then, depending on how the research question is framed, the frequency map shows different results. From Figure 25, it can be argued that most heatwave events occurred over the eastern part of Europe when the accumulated area contours are used. With this method, a heatwave is counted once independently of its duration. Moreover, it can be deduced from these results that most contours in the tropics (in Figure 10) belong to a few long-lasting heatwaves, confirming the findings from Figure 11. It is important to note the distinction between the two, especially since it is typically heatwave events (where each heatwave are represented by a single value) that are analyzed to discern trends in heatwave characteristics (e.g., Luo et al. [2022], Perkins and Alexander [2013]).

The three characteristics explored in Section 4.2.1 revealed different patterns. Based on Figures 11, 12 and 13a, it can be observed that the regions experiencing the longest heatwaves are also the regions experiencing the largest ones. In contrast, the small heatwaves are typically associated with shorter durations (west of North America, WCS, Arabian Peninsula and Siberia). More generally, the median duration and the average size of heatwave for each grid point in the Northern Hemisphere can be deduced. For example, the median duration of a heatwave over Central Europe is 7 or 8 days, and its average size is about 5 or 6×10^6 [km^2]. For instance, Luo et al. [2024] have found a median duration of 10.2 days and an average

size of 7.32×10^6 [km^2] over the Eurasian continent. More generally, this analysis suggests that the results from Luo et al. [2024] overestimate the size and duration of heatwaves over North America and Eurasia and underestimate those characteristics over Africa. The metric they used to account for size was the accumulated area in contrast to the individual contour size used here. Despite this difference, the average spatial extent explored here is larger than in their study. However, both latitudinal profiles (Figure 12 b) in this thesis) show similar magnitude at high latitudes where it is mostly land (between 60°N and 70°N). Furthermore, the duration in China seems to be overestimated by 2 days in this study in comparison to Luo et al. [2022]. They found most heatwaves to have a median duration of 3 or 4 days while the median duration in this analysis is mostly 5 or 6 days over China. The results from Luo et al. [2022] are exclusively over China which makes direct comparisons difficult. However, the shorter duration makes sense as it is likely that heatwaves began and ended outside this region but their analysis only captured the time steps of the same heatwaves that occurred over China, thereby omitting their start and end points that occurred outside.

This analysis was the first time ConTrack was used to track warm temperature anomalies. Section 4.1.1 shows that the tracking algorithm is able to track heatwaves in the Northern Hemisphere based on a case study. Rogers et al. [2022] explored the behavior of large concurrent heatwaves in the Northern Hemisphere during the warm season (MJJAS). To do so, they defined a heatwave as a period of 3 or more consecutive days with a daily mean temperature at the 2m level greater than the local 90^{th} percentile. Additionally, they set a minimum size criteria of 1.6×10^6 [km^2] and the percentile is based on the 1981–2010 climatology. This definition is very close to what was used in this analysis (Section 3.2) except for size criteria and the use of a climatology as a reference. Interestingly, the first figure from their analysis displays where the heatwaves they identified were located on 30 July 2018. In comparison, the output of ConTrack is very similar for that day (Figure 32). Heatwaves over North America and Europe showed a good match, while the main differences are likely due to the different tracking tools and/or the different reference for the intensity threshold. This demonstrates that the contours tracked by ConTrack are comparable to what other studies have found.

Section 4.1 showed the speed of heatwaves in the characteristics. It was calculated based on the center of each individual contour. It would be possible to calculate a similar result to Section 4.2.1 for the speed too. However, it is worth noting that at times, ConTrack identifies individual contours with a "double blob" configuration, where two distinct blobs belong to the same individual contour at a given time step. For example, if the purple contour in Figure 2 (left) is considered, it would show two contours instead of one. The coordinates of each individual contour are deduced by their center of mass. Consequently, under these conditions, the coordinate of the center of the "double blob" lies outside of the individual contours. This issue is exacerbated when the "double blob" configuration occurs at the periodic boundary conditions at the 180°E/180°W longitude transition. The center of mass would be positioned

in between the two contours somewhere around longitude 0°. Therefore, the calculation of the speed between time steps based on those coordinates would be incoherent. As there is not an easy fix to this problem, I have chosen not to include the result for speed, as this feature would skew the statistics. However, one could rewrite the function in the ConTrack python package to account for the merging and splitting of individual contours and to solve the issue where the center of mass shows incoherent coordinates. Then, the average speed of heatwaves in the Northern Hemisphere could be calculated. Furthermore, exploring the frequency and potential impact of heatwave merging and splitting could reveal distinctive characteristics associated with these phenomena.

In my analysis, large contours (both individual and accumulated area contours) exert a greater influence than smaller ones. During the calculations, larger contours possess a larger spatial extent, thereby amplifying their impact on the spatial distribution (e.g., Figures 10,11, and 12). Consequently, the characteristics of large contours are favored in the results. This could explain why large and long-lasting heatwaves characterize the top of South America (Figures 11 and 12), even though this region is not especially prone to such traits (Luo et al. [2024]). Luo et al. [2024] have found an average size and median duration for heatwaves over South America of 5.77×10^6 [km^2] and 8.47 days, respectively. In this case, my results suggest that these estimates are underestimated, as it was found that the size of heatwaves is about 12-16 $\times$ 10^6 [km^2] and the median duration is longer than 10 days. Figure 10 reveals a low frequency over that region and Figure 12 exerts an average size larger than the region itself suggesting that heatwaves occurring over that region are usually part of very large heatwaves. Additionally, most of the heatwaves detected by ConTrack last 3 or 4 days (Figure 16) but only a few regions show such median duration in Figure 11. In contrast, a smaller proportion of long-lasting heatwaves is identified (Figure 16), but a longer median duration is common in Figure 11. This effect is attributed to long-lasting heatwaves, which are typically associated with large contours, while short-duration heatwaves are usually linked to small contours (Figure 13a). This analysis is capable of capturing such a wide range of contour sizes because it doesn't enforce a minimum size requirement unlike Stéfanon et al. [2012] or Rogers et al. [2022]. Moreover, the size of individual contours changes during the lifetime of heatwaves (Figure 13b). Based on Figures 26 and 27 it can also be deduced that the regions where heatwaves originated differ from the regions where they terminated. These Figures reveal the difference in size between the first and the last days of heatwaves by exhibiting a different count frequency, despite considering the same number of individual contours in the calculations.

4.3 Impact of ENSO Conditions on Heatwave Size

4.3.1 Results

More than 60 events per year are recorded during El Niño summers while it is usually below that threshold for La Niña summers except in 2000, 2021, and 2022 (Figure 4). In total 920 heatwaves were identified during El Niño summers, whereas only 755 were detected during La Niña summers (Figure 4). That difference is about 14 events per year and a lower number of heatwaves during La Niña is coherent with what previous studies have found (e.g., Lin et al. [2018]; Pai et al. [2022]). Similarly to Figure 10, I decomposed the frequency for El Niño, La Niña, and neutral conditions. Adding up the frequencies from these three maps would yield Figure 10. During El Niño summers, more heatwaves were tracked than during La Niña summers. This difference is observable in Figure 14. In contrast, the frequency during neutral ENSO conditions looks similar to the overall frequency shown in Figure 10 as 40 out of 65 summers are considered.

The spatial distribution of heatwaves during El Niño years exhibits notable differences compared to the overall period. The characteristic band of SST anomaly over the tropical Pacific Ocean (Scaife et al. [2017]) observed in Figure 10 appears relatively smaller during the selected El Niño summers than during neutral conditions (Figure 14). It is important to note that the definition used in this analysis relies on the Oceanic Niño Index during the winter months. Consequently, there is a possibility that summers experiencing El Niño conditions (when the ONI is greater than 0.9°C during JJA) may be classified as neutral in this study, hence explaining the observed discrepancy along the coast of South America. The Caribbean Sea and the West of the Atlantic experience more heatwaves during the El Niño years. In contrast, similarly to what was observed in Figure 10 India and the Arabian Sea experienced frequent heatwaves. In contrast, only a few were detected over the central Pacific. More generally, the higher latitudes are experiencing fewer events during El Niño summers. In contrast, during La Niña summers, there are two frequency maxima: one in the northern Pacific and another in the region of the Azores High. Additionally, there are very few heatwaves occurring in low latitudes during La Niña summers compared to El Niño summers.

This difference can be attributed to the presence of upper-level height anomalies over these regions during El Niño, which typically induces a hot and dry atmosphere through anomalous subsidence, creating favorable conditions for the occurrence and persistence of heatwaves, as suggested by Wu et al. [2024]. Additionally, during El Niño, the Walker circulation weakens significantly over the Pacific Ocean (DiLiberto et al. [2014]; Stocker et al. [2020]; Wu et al. [2024]). The strong rising motion shifts to the central Pacific, while the sinking branches move over South America and Southeast Asia. Consequently, regions associated with these anomalous sinking branches typically experience anomalous dry and

hot conditions (DiLiberto et al. [2014]; Lin et al. [2018]; Stocker et al. [2020]; Wu et al. [2024]). Moreover, Kenyon and Hegerl [2008] have found that there are warmer temperatures over India during El Niño. Then, based on the modulation of the Walker circulation, there are regions experiencing more favorable conditions for heatwaves to develop, and ConTrack has tracked most heatwaves during El Niño summers at those locations (Figure 14). Therefore, these favorable conditions lead to higher frequency (Figures 4, 14) and longer heatwaves (Wu et al. [2024]).

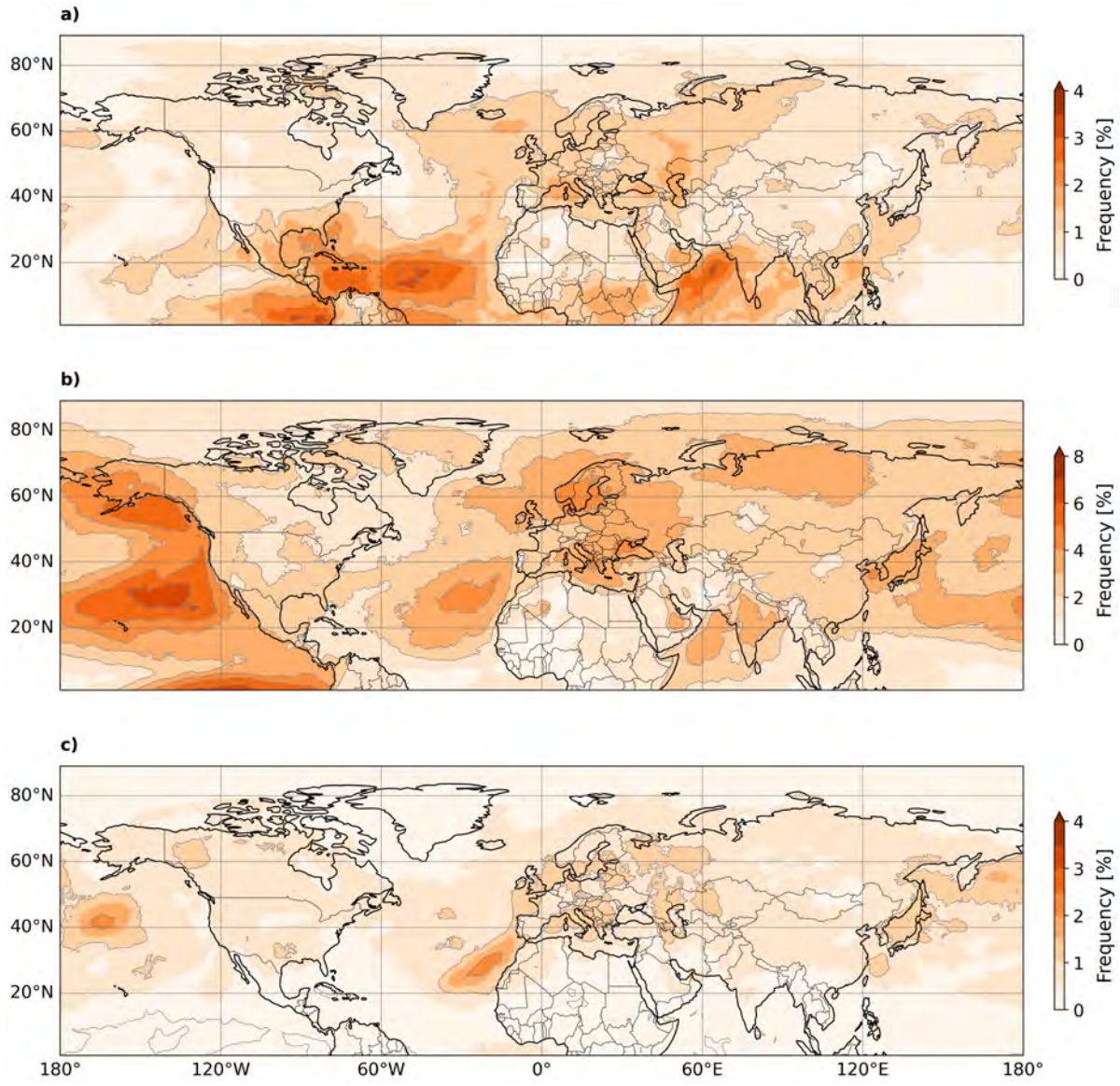

Figure 14: Northern Hemisphere JJA* heatwave (individual contours) frequency during the 12 El Niño summers (**a**), the 40 neutral ENSO summers (**b**), and the 13 La Niña summers (**c**). Note the different colorbar for **a)** and **c)**.

Additionally, El Niño conditions appear to influence the size of heatwaves in the Northern

Hemisphere (Figure 15). Red shading indicates areas where the average size of heatwaves during El Niño summers was larger, while grey shading indicates areas where the average size was smaller. Interestingly, regions around the Caribbean and the eastern Pacific identified in Figure 14 a) do not show a distinctive pattern. Many heatwaves are detected in these areas, but their size does not seem to be influenced by El Niño conditions. In contrast, the size of heatwaves is larger over most of South Asia when a mature El Niño stage precedes the summer. A large grey area along the west coast of the United States indicates that the few heatwaves detected in this region were smaller during El Niño summers. This region ranks among the lowest calculated values (hatched), with only a small portion appearing to be statistically significant (dotted). Additionally, a large area between Siberia and China shows minimal difference, as does the Atlantic region along the Moroccan coast. In Eastern Europe, the size of heatwaves appears larger, although statistical significance is confined to a small area.

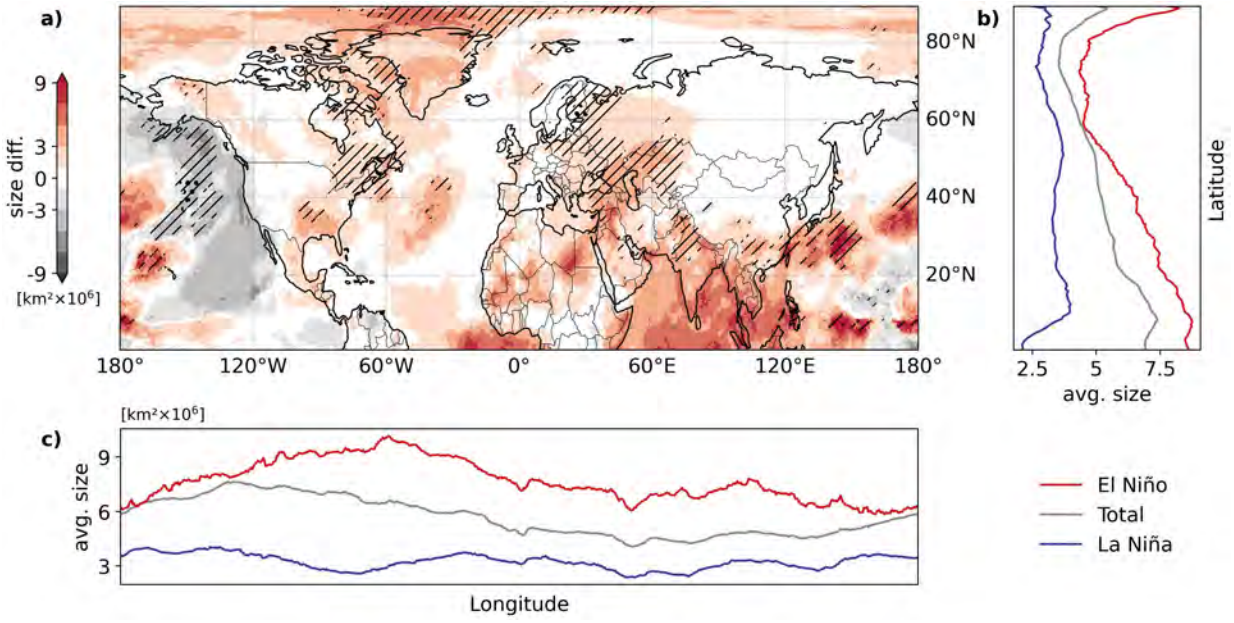

Figure 15: **a)** Composites of heatwave average size during the 12 El Niño summers minus heatwave average size during the total period (1959-2023) for the Northern Hemisphere. Hatching shows where values are in the 5% lower or 5% higher range based on their ranking. Dots indicate areas statistically significant at the 10% level. **b)** Mean average size with latitude during El Niño conditions (in red), La Niña conditions (in blue), and during the total period (in grey). **c)** same as b) but for longitude.

Both the longitudinal and latitudinal profiles (Figure 15 c and b) show that heatwaves are larger during El Niño summers. Each line represents the average size during El Niño (red), La Niña (blue), and the entire period (grey). Conversely, heatwaves are smaller during La Niña summers.

4.3.2 Discussion

There are several ways to define El Niño summers, such as selecting different indices or reference seasons (e.g., JJA instead of DJF). Moreover, it is possible to distinguish between the intensity of ENSO conditions, as shown in Reddy et al. [2021]. Additionally, they considered ENSO years in conjunction with other concurrent climate modes. Therefore, the results presented here are based on the selection made in Section 3.4, and different definitions would likely yield different results.

A higher frequency of heatwaves is observed during El Niño summers and a lower one during La Niña summers (Figures 4 and 14), consistent with the findings of Wu et al. [2024]. With a lag of approximately 6 months (between DJF and JJA), the frequency pattern aligns with the results of Trenberth et al. [2002], over regions where generally higher surface temperatures are associated with El Niño, except over the NWP. Additionally, the frequency of heatwaves over India, the West of Asia, and the Caribbean corresponds to the increase of warm days revealed in Kenyon and Hegerl [2008] during El Niño conditions. More specifically, the frequency of heatwaves over India, the Indochine Peninsula, and the West of China is coherent with what has been found (Lin et al. [2018]; Luo and Lau [2019, 2020]; Pai et al. [2022]). A warmer Indian Ocean may also be observed under El Niño conditions (Brönnimann [2007]; Figure 28), which may explain the high frequency of heatwaves over the Arabian Sea. Additionally, the low frequency of events in the central Pacific is expected due to increased convective activity, while the high frequency on both sides of the Pacific can be attributed to the drier conditions that prevail during El Niño (Davey et al. [2014]; DiLiberto et al. [2014]). More generally, a higher frequency of heatwaves was observed where the SST was warmer during El Niño summers (Figure 28). This analysis focuses on the influence of ENSO on heatwave size, but it is also likely that other climate modes have influenced surface temperatures at certain locations and thus impacted the results.

Reddy et al. [2021] investigated the influence of co-occurring modes of ENSO and IOD on large heatwaves in Australia. Their results indicate that the size of heatwaves is larger during strong El Niño events. Australia typically experiences drier conditions (west of the Pacific) during El Niño (Davey et al. [2014]). Additionally, they found that heatwaves were smaller during La Niña conditions, corroborating the findings shown in Figure 29. Similar to these findings, my results suggest that heatwaves are larger in regions with favorable conditions for temperature rise during El Niño, particularly in South Asia, although the statistical significance is limited. This could potentially lead to larger affected areas during those summers. Additionally, since the intensity threshold used with ConTrack seems to directly influence the size of heatwaves (Figure 23), it would be interesting to observe if more intense and/or longer heatwaves exhibit a different response due to El Niño. For instance, with the tracking algorithm used in Wu et al. [2024], a higher intensity threshold reduced the sample

size but did not influence the relationship between heatwaves and ENSO. Furthermore, my result does not imply that La Niña summers are less hazardous in terms of heatwaves, as regional relationships vary depending on ENSO phases (Kenyon and Hegerl [2008]). Notably, one of the recent most intense heatwaves occurred in 2021 (Section 4.1.1) during La Niña conditions.

5 Conclusions & Outlook

In this thesis, I investigated general characteristics of heatwaves in the Northern Hemisphere from 1959 to 2023 using a tracking algorithm originally developed to study atmospheric blocking, ConTrack.

I have shown that ConTrack tracks heatwaves in a meaningful way with the criteria chosen. The individual contours identified for the 2021 Pacific Northwest heatwave fit well within the atmospheric conditions during which the heatwaves developed, although rapid size increases and decreases were not captured with the overlap criteria chosen (Section 4.1.1). Additionally, when I focused on the WCS region, I attributed the detected heatwaves to specific phenomena known as heat lows, given their characteristics (4.1.2). Then, I calculated the frequency, average size, and median duration of heatwaves (4.2). It was found that heatwaves occur at preferred locations in Figure 10. The frequency maxima over the PNW and north of Europe were linked to blocking occurrences. In contrast, the maxima along the west coast of the USA and over the Azores were associated with persistent high-pressure systems, the North Pacific High and the Azores High, respectively. In addition, the maxima over the central Pacific resembled the SST anomaly pattern associated with El Niño. The frequency maxima in the WCS were linked with heat lows, as was likely the case for the maxima in the Arabian Peninsula. Next, this thesis showed that the longest heatwaves occur in Central America, in the Atlantic and Pacific Oceans, while the shortest take place in North America, Siberia, the western equatorial Pacific, Southeast Asia, WCS, and the Arabian Peninsula (Figure 11). Then, it was illustrated that the largest heatwaves occur in the central Pacific, Caribbean Sea, east of the Atlantic, and in some regions over Africa. The smallest heatwaves mostly occur over land in North America, north of Europe, Central Sahara, Arabia, and Siberia (Figure 12). This thesis evidenced that the longest heatwaves are generally also among the largest. Lastly, I investigated whether ENSO conditions affect the size of heatwaves (Section 4.3). This thesis showed that the frequency of heatwaves has different patterns depending on the ENSO conditions (Figure 14). Then, it was found that heatwaves tend to be smaller in the Pacific Northwest, and larger in South Asia, Eastern Europe, and western North America during El Niño conditions, albeit with limited statistical significance (Figure 15). Conversely, during La Niña conditions, heatwaves generally exhibit smaller sizes.

The tracking of heatwaves with ConTrack has shown interesting results but I believe the use of this tool for heatwaves tracking has not yet reached its full potential, and there is still more to explore. In addition to the proposal made in Section 4.2.2 to account for the merging and splitting of individual contours, here are several suggestions for further investigation in future studies.

- **Additional characteristics:** Thanks to ConTrack, I calculated the frequency, dura-

tion, and size of heatwaves in the Northern Hemisphere. However, similar results for additional characteristics such as the speed (only if ConTrack code is modified) and the total distance heatwaves have traveled. It could also be possible to investigate the direction of travel of heatwaves (as in Luo et al. [2024]). Additionally, this thesis did not address the intensity of heatwaves and it would be worth the exploration. Therefore, these additional results would offer a more complete picture of the characteristics of the tracked heatwaves. For example, the direction of travel of heatwaves over Europe is mainly to the East (Luo et al. [2024]) but maybe the few ones going to the West would reveal specific characteristics in Size and/or intensity. Moreover, my thesis was limited to the Northern Hemisphere, but it could be extended to the Southern Hemisphere and considering both boreal and austral summers.

- **Temperature anomaly:** In this analysis, Contrack tracked heatwaves based on a temperature anomaly field where the daily mean temperature was standardized using a centered 31-day, 9-year running window. It removed the seasonality and the trend. However, using a climatology as a reference period to deduce the temperature anomaly retains the long-term trend in the data. Therefore, it would be possible to explore the trends in heatwave characteristics as in Luo et al. [2024] and Rogers et al. [2022], to investigate if they have changed in the past decades.

- **Heatwaves and blocking relationship:** There exists a strong relationship between atmospheric blocking and extreme temperature over the mid-latitudes in the Northern Hemisphere (Chan et al. [2022]; Pfahl and Wernli [2012]). A similar analysis to Pfahl and Wernli [2012] could be conducted using ConTrack to identify both blocking situations and heatwaves, thereby assessing the frequency of co-occurrence between heatwaves and blocking events.

- **Heatwaves and climate modes relationship:** Heatwaves in many regions are influenced by climate variability modes, which alter atmospheric background conditions and thus favor the development and amplification of heatwaves (Wu et al. [2024], Section 4.3). It would be worth exploring whether different responses exist based on the intensity of climate modes, as in Reddy et al. [2021] who distinguished between strong and moderate conditions for ENSO and IOD. They looked at the different responses when these climate modes interact with each other. For example, they assessed the specific impact on heatwave size when a strong El Niño occurs simultaneously with a moderate IOD negative. Since they focused on Australia, expanding the analysis over both hemispheres during both boreal and austral summer would yield broader insights into heatwave interactions with climate modes. Additionally, a similar analysis to Section 4.3 with other parameters such as duration could be conducted.

- **Heatwaves detection in climate models:** Heatwaves are projected to increase in both intensity and frequency (Perkins [2015]; Seneviratne et al. [2021]). Studies have explored both temperature and heatwave frequency increases in climate models (e.g., Fischer and Schär [2010]), but it would be interesting to analyze how the characteristics identified with ConTrack would evolve. Thus, I would compare the outcome of an analysis with ConTrack for both historical and future time periods from model simulations.

- **Atmospheric and Marine Heatwaves co-occurrence:** The temperature change at the ocean surface is influenced by various processes, including net sea-air heat exchange (net incoming longwave and shortwave radiation, and net latent and sensible heat fluxes), vertical diffusion, and mixing (Vogt et al. [2022]). An analysis of the co-occurrence of atmospheric and marine heatwaves (similar to Aboelkhair et al. [2023]) could be conducted over a larger region.

A Appendix: Sensitivity Analysis

This section outlines the various steps I took to determine the most suitable set of parameters for using ConTrack with surface temperature. The primary objective was to obtain sufficiently coherent contours representing heatwaves for analysis.

A.1 Duration

ConTrack works in a straightforward way. It first identifies the individual contours that meet the intensity threshold requirement. Then, it looks for those respecting the 50% overlap criteria between time steps. Lastly, it applies the persistence filter (minimum duration).

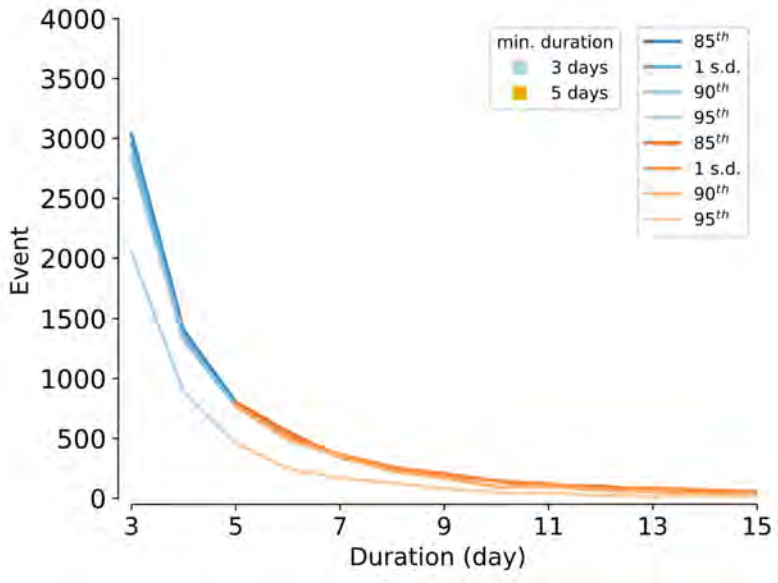

Figure 16: Number of heatwaves identified by ConTrack based on different intensity thresholds (the 85^{th} percentile, one standard deviation, 90^{th} percentile, and 95^{th} percentile represented in dark to light shades) and different minimum durations (with a minimum of 3 days in blue and a minimum of 5 days in orange) between 1959 and 2023 during JJA*.

Two minimum durations were tested, 3 days and 5 days as suggested by other studies (Perkins [2015]). Figure 16 shows the number of heatwaves in function of their duration. The majority of heatwaves are short-lived and their number decreases exponentially for longer duration. Thus, independently of the intensity threshold (the color shading of the lines), most heatwaves detected are short-lived. The results depicted in Figure 16 show that when a minimum of 5 days is considered, it is essentially a subset of the results obtained with a minimum of 3 days. The only difference lies in their duration, as the contours identified remain the same. Therefore, I set the minimum duration to 3 days to ensure an adequate sample size aligning with the methodologies of other studies (e.g., Böhnisch et al. [2023], Rogers et al. [2022]).

A.2 Smoothing

The tracking algorithm searches for continuous areas meeting specific criteria. However, surface temperature can be challenging to work with (especially at 0.5° resolution) as it exhibits high spatial variability. As a result, the contours were rarely continuous (as observed in Figure 22 in purple) and their interpretation was not obvious. Additionally, ConTrack detected numerous very small and localized events, as well as unwanted artifacts, that were undesirable. Tamarin-Brodsky et al. [2020] likely selected a coarser resolution to minimize this noise. Thus, one possibility to improve the dataset was to also opt for a coarser resolution. However, I believed the analysis could benefit from having a finer resolution.

Therefore, a common method used (e.g. Schwierz et al. [2004]) consists of smoothing field data over time. Consequently, rolling windows of 3 and 5 days were computed to have a smoother field. As the first intermediate results emerged, it looked like it was artificially increasing the size and duration of heatwaves detected. As a result, this method was not further investigated.

Another method consisted of smoothing out the data spatially. The idea is to consider the value of neighboring grid points to average the field. This operation was carried out with the smoothing function from Kaderli [2023]. They used it with their algorithm to detect Rossby Wave Breaking (RWB) more easily. The number of neighboring grid points to consider and their weights are specified via a matrix when computing the field average.

Consequently, 5 different matrices were tested. The first one used the default selection from Kaderli [2023] (RWB) where they considered a 5-point smoothing (not diagonally) with a double-weighted center. For the second and third ones, the range was expanded from 5 to 9 grid points (one at the center plus the 8 surrounding ones). This is labeled as the 9-cell smoothing. Figure 17 represents the three first different weight combinations used: RWB, Inverse Distance Weighting (IDW) (Hartmann et al. [2023]), and linear (closest points' weights divided by 3 and 4.5 diagonally)

0	0.5	0
0.5	1	0.5
0	0.5	0

a) RWB

0.35	0.5	0.35
0.5	1	0.5
0.35	0.5	0.35

b) 9-IDW

0.22	0.33	0.22
0.33	1	0.33
0.22	0.33	0.22

c) 9-linear

Figure 17: Representation of the different weights matrices computed for the 9-cell smoothing.

Then, the two latter were expanded to consider an extra layer of grid points around the center. It means 16 new points were considered in addition to the previous 9. This is labeled the 25-cell smoothing. The horizontal and vertical furthest points are in this case distanced by two from the center. For the linear method, the four corners grid points were set to zero

and the weights of the remaining points were divided by 9. For the IDW, another layer was added based on the same calculation. These two matrices are displayed in Figure 18.

0.18	0.22	0.25	0.22	18
0.22	0.35	0.5	0.35	0.22
0.25	0.5	1	0.5	0.25
0.22	0.35	0.5	0.35	0.22
0.18	0.22	0.25	0.22	18

a) 25-IDW

0	0.11	0.22	0.11	0
0.11	0.22	0.33	0.22	0.11
0.22	0.33	1	0.33	0.22
0.11	0.22	0.33	0.22	0.11
0	0.11	0.22	0.11	0

b) 25-linear

Figure 18: Representation of the different weights matrices computed for the 25-cell smoothing.

As a result, five different datasets representing the same temperature field were computed. To compare them, the same parameters (90th percentile, 50% overlap, minimum 3 days duration) were applied. Then, the RWB smoothing was not considered viable because the results were not significantly different from the 'default' data. The different outputs were compared by calculating the frequency as shown in Section 3.3. Each result was subtracted from another to observe if there were any spatial differences between them. The result for 9-IDW minus 9-linear is shown in Figure 19, while Figure 20 shows 9-IDW minus 25-IDW. The remaining comparisons are not shown here.

Figure 19 reveals very little difference between the two 9-cell smoothing methods. Based on these observations, the different weighting methods were considered equivalent, indicating that the varying weights had a limited impact on the outcome. However, Figure 20 shows the difference between 9-IDW and 25-IDW. Most regions had a higher frequency (in red) using the 9-cell smoothing method compared to the 25-cell method. A similar pattern was observed when comparing 9-linear with 25-linear. Therefore, two things were concluded. First, when comparing both 9-cell and 25-cell smoothing, the respective weights have a limited influence. Second, larger differences emerged when comparing 9-cell to 25-cell smoothing, regardless of the weight values. As a result, both 9-linear and 25-linear were excluded from considerations, retaining only the IDW method.

Next, the average size of the identified individual contours and their numbers for each method were examined. Fewer contours were expected with 25-cell smoothing for two reasons. First, this method reduces noise by eliminating localized and small-scale events. Second, the smoothing effect can cause two nearby events to be considered as a single event.

These hypotheses were verified, as shown in Figure 21. The average size for data without smoothing is small, while the average size increases with smoothed data. It can be noted that the heavier the weights, the larger the average size becomes. Similarly and because both results are interconnected, the number of identified events decreased due to the different smoothing applied. The closest resemblance to the original data was observed when using the default parameters from Kaderli [2023] (RWB). However, he used a coarser resolution

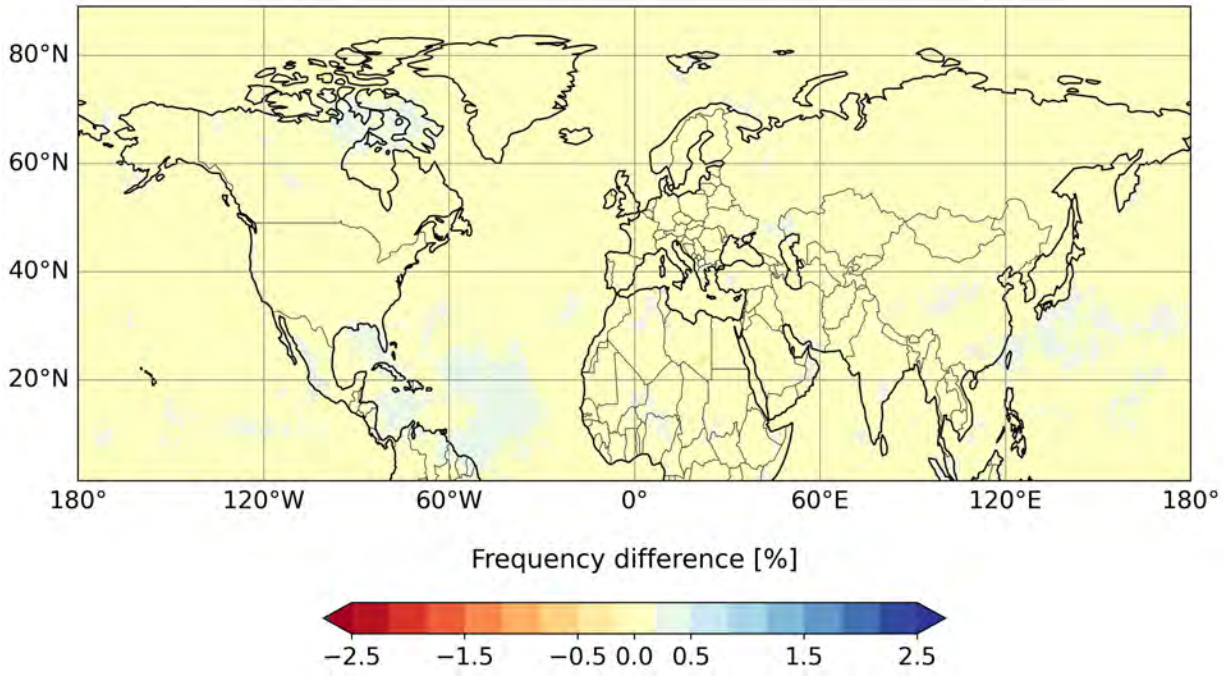

Figure 19: Difference of frequency between 9-IDW and 9-linear as calculated in Figure 10.

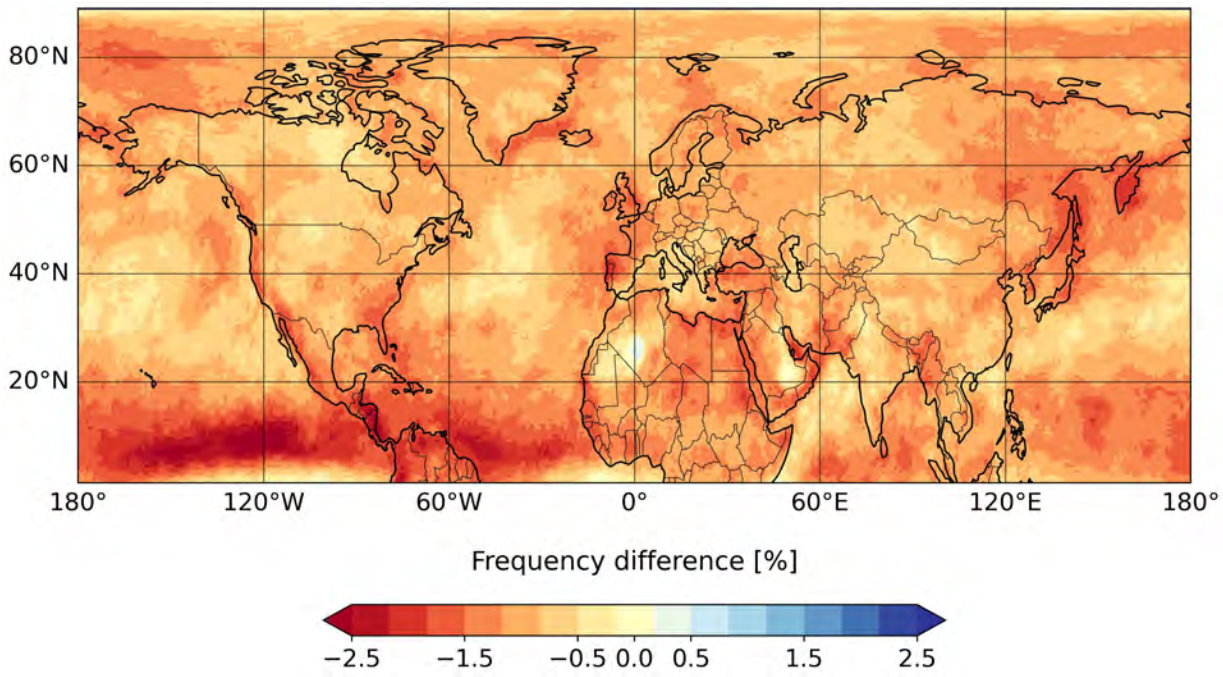

Figure 20: Similar to Figure 19, but it shows the difference between 9-IDW and 25-IDW.

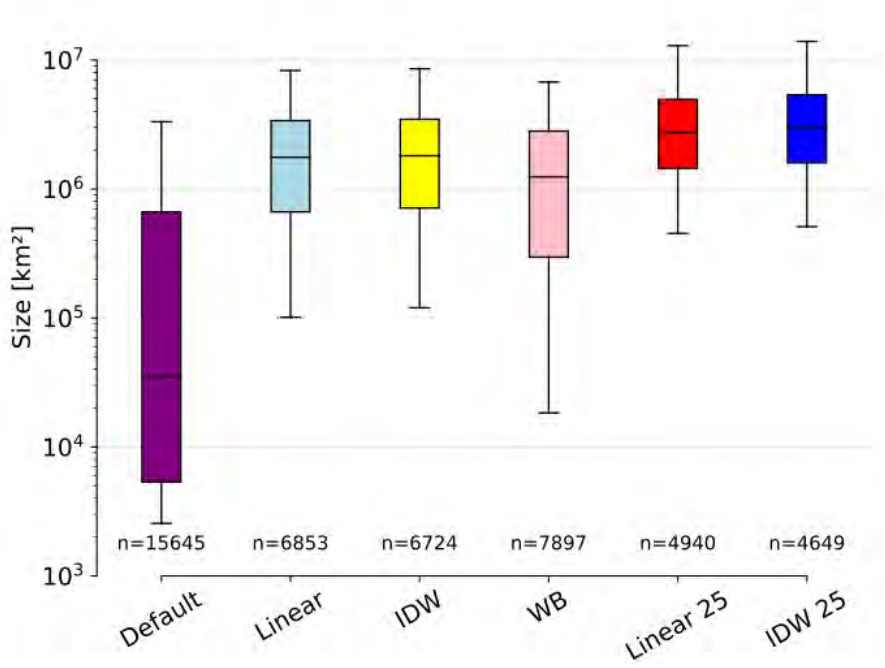

Figure 21: Size distribution of all individual contours detected in MJJAS from 1959 to 2023 obtained from the different smoothing methods. default (purple), 9-lin (light blue), 9-IDW (yellow), RWB (pink), 25-lin (red) and 25-IDW (blue). N is the number of heatwaves detected for each field.

and different variables. For these reasons, and upon manual inspection of the outputs, it was excluded from further investigations. At this stage of the analysis, only 9-IDW and 25-IDW remained for consideration, while the default data served solely as a reference for comparison.

In addition to observing metrics such as size via boxplots and frequency calculations, the outputs for each smoothed field were manually assessed. For instance, Figure 22 shows the same heatwave with individual contours representing the results for each dataset. It can be observed how default data (in purple) differs from the smoothed fields. The default contour appears more jagged and harder to interpret. In contrast, the individual contours for 9-IDW and 25-IDW appear more coherent due to the applied smoothing.

After further investigations of both datasets, I decided to exclude 25-IDW. Although the sizes of heatwaves are larger when considering 25-IDW, suggesting it may perform better in some aspects (such as the shape), other factors led to its exclusion. For example, when two close events are combined together instead of being correctly classified as different ones. This might have a great influence on the results and this effect is less prominent for 9-IDW. In the end, I found that 9-IDW was performing efficiently: it maintained a good sample size and had a lesser influence on the overall field.

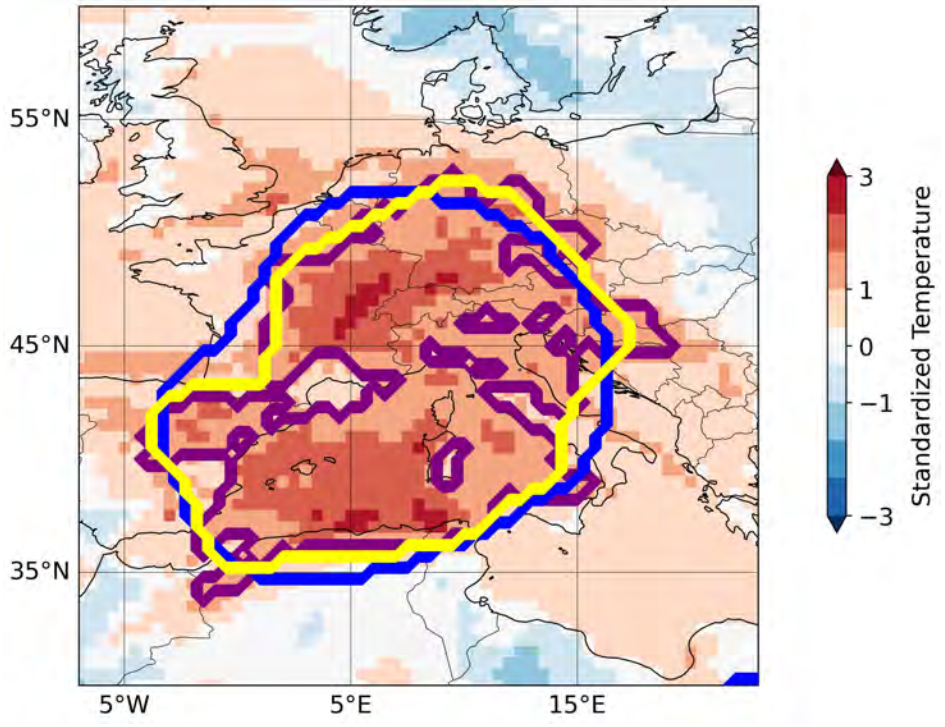

Figure 22: Contours identified on the 23.06.2003 with 3 different smoothed fields. Default in purple, 25-IDW in blue, and 9-IDW in yellow. The background shows the default standardized temperature anomaly field.

A.3 Intensity Threshold

Lastly, different temperature thresholds were experimented with. First, it was not possible to use a fixed value threshold due to the high spatial variability of surface temperature between equatorial and polar regions (Ouyang et al. [2023], Figures 30 and 31).

Since surface temperatures exhibit high spatial variability between equatorial and polar regions (Ouyang et al. [2023]; Figures 31 and 30), using a fixed threshold value over the Northern Hemisphere was not possible. To address this variability, an approach based on percentiles was adopted where each grid point's local percentile was calculated. Then, four different percentile thresholds based on the standardized temperature were tested. They are respectively the 85^{th} percentile, 90^{th} percentile, 95^{th} percentile, and one standard deviation, and each of them is processed as described in Section 3.2. Their frequency is shown in Figure 24.

In Figure 23, it can be observed that the more restrictive the threshold was the smaller the events got. There was a significant drop in identified events while considering the 95^{th} percentile. On the contrary, the 85^{th} percentile did not differ enough from one standard deviation and it was removed from consideration. Then, between one standard deviation the 90^{th} percentile, I decided to go for the latter as it is a common threshold in usage when studying heatwaves (e.g., Beobide-Arsuaga et al. [2023]; Chan et al. [2022]; Stéfanon et al.

[2012]), which would allow the results to be more relatable to other studies.

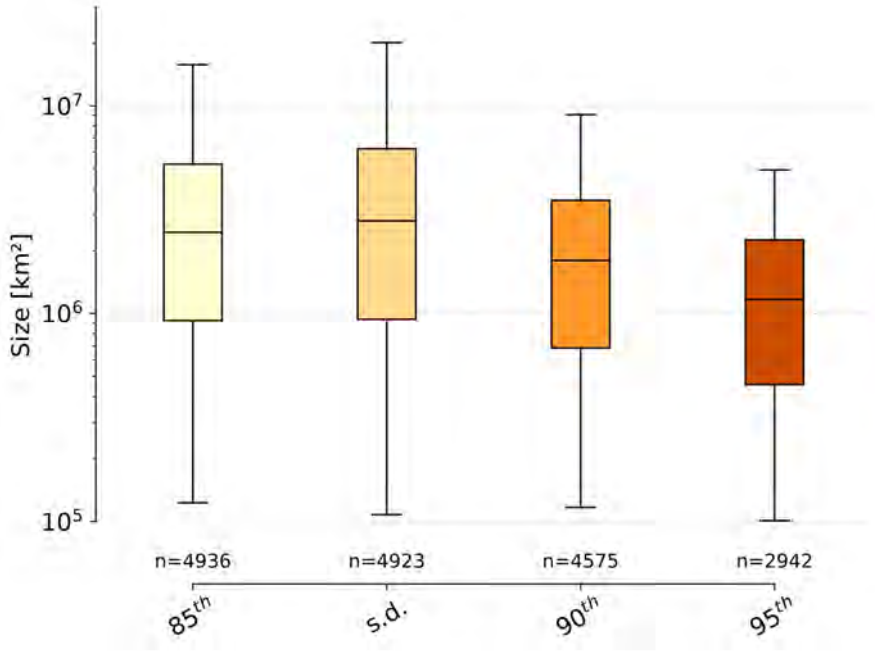

Figure 23: Size distributions of heatwaves in Northern Hemisphere from 1959 to 2023 during JJA* based on 4 different thresholds from the lightest to darkest shade: 85^{th}, one standard deviation, 90^{th}, and 95^{th} percentile.

A.4 Comments

The speed and shape of heatwaves imply some challenges in assessing the ideal set of parameters to use with ConTrack. Issues can be identified for a few numbers of heatwaves, but the number analyzed in this thesis does not allow such specific treatment. One example can be the influence of large areas of inland water for the events detected by ConTrack. Variations in temperature happen more rapidly over land than over sea. These pools can experience some warming in line with their surroundings. However, the region around can become colder than on average quickly. It means the water masses radiate the accumulated energy back into the atmosphere during such strong variations. Thus, the warm anomalies calculated match exactly the size of the water extent. As a result, ConTrack detects contours of events where the location and the size do not change. Those are usually short and small-scale events. It could also partially explain why the results for the 95^{th} percentile are systematically smaller, especially in the default data where such events have the largest proportion.

Thus, it is recognized that the selection process was not flawless and involved acceptable trade-offs. Nevertheless, I aimed to examine an adequate number of heatwaves to discern distinct signals. These considerations guided my decision to conduct the analysis using the 90^{th} percentile as the intensity threshold derived from standardized temperatures, with a

minimum duration of 3 days. Additionally, while I did not explore alternative variations, I am confident that preserving a 50% overlap does not compromise the quality of the results.

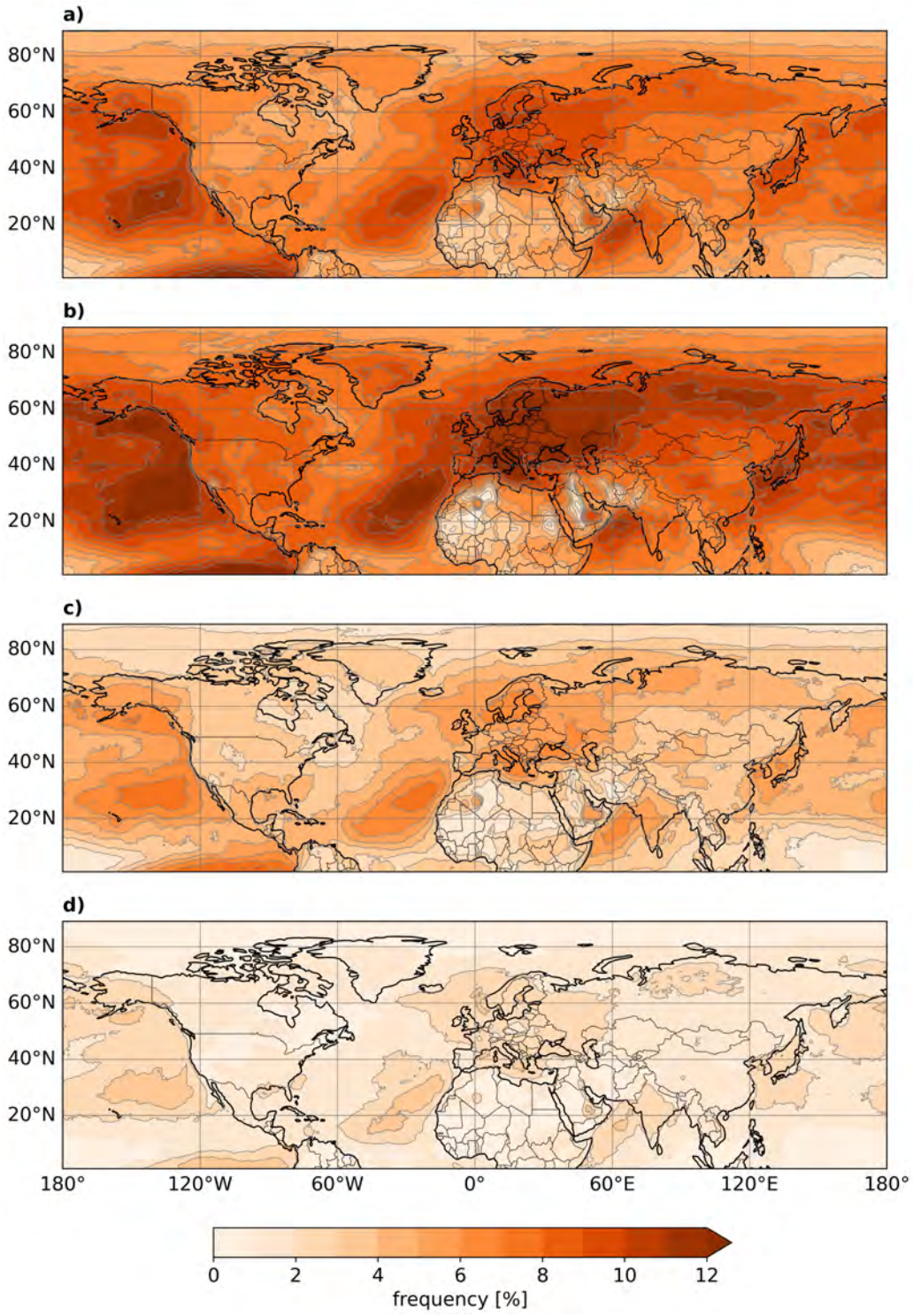

Figure 24: Same as figure 10 but showing the frequency for four different intensity thresholds. **a)** 85^{th} percentile, **b)** one standard deviation, **c)** 90^{th} percentile, **d)** 95^{th} percentile. Note the different colorbar than in Figure 10.

B Appendix: Additional Results

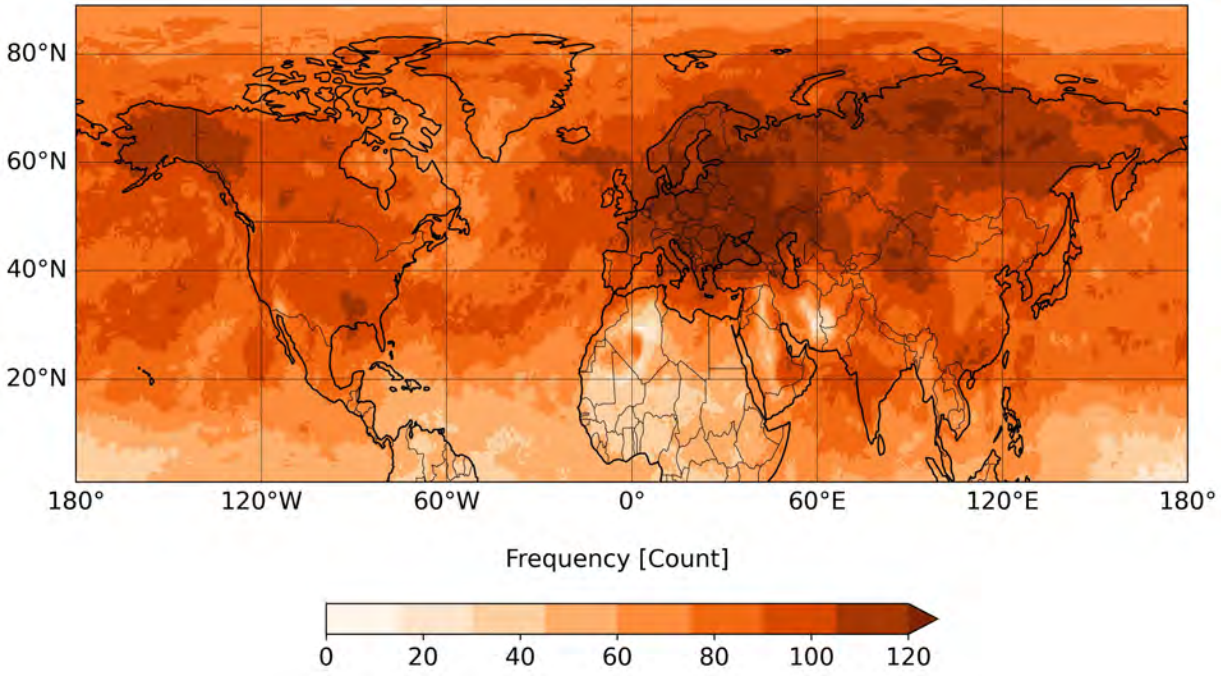

Figure 25: Northern Hemisphere JJA* heatwave (accumulated area contours) frequency from 1959 to 2023.

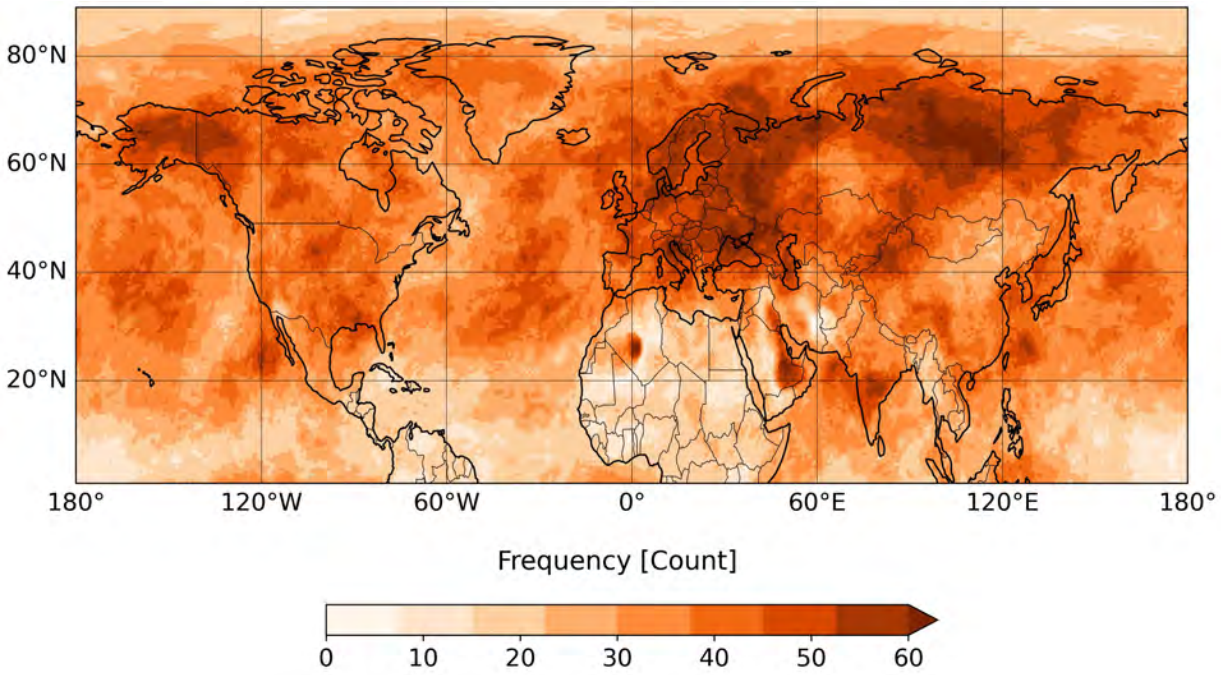

Figure 26: Northern Hemisphere JJA* heatwave genesis day (only the first individual contours of each event) frequency from 1959 to 2023.

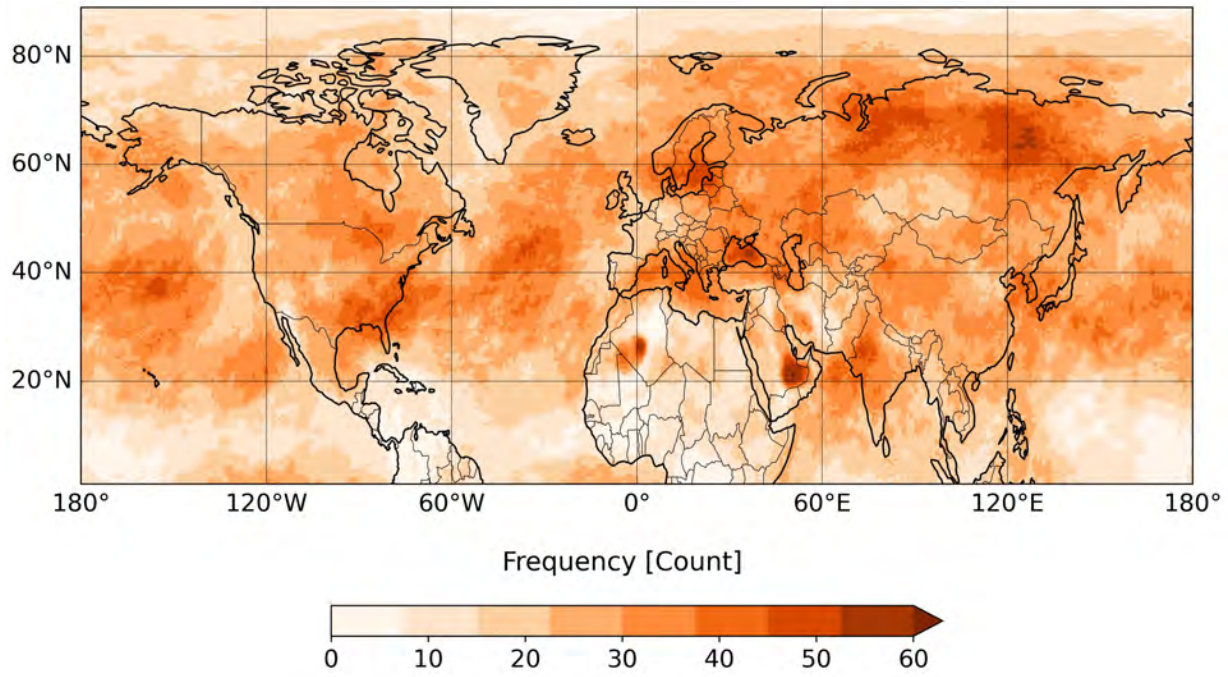

Figure 27: Northern Hemisphere JJA* heatwave lysis day (only the last individual contours of each event) frequency from 1959 to 2023.

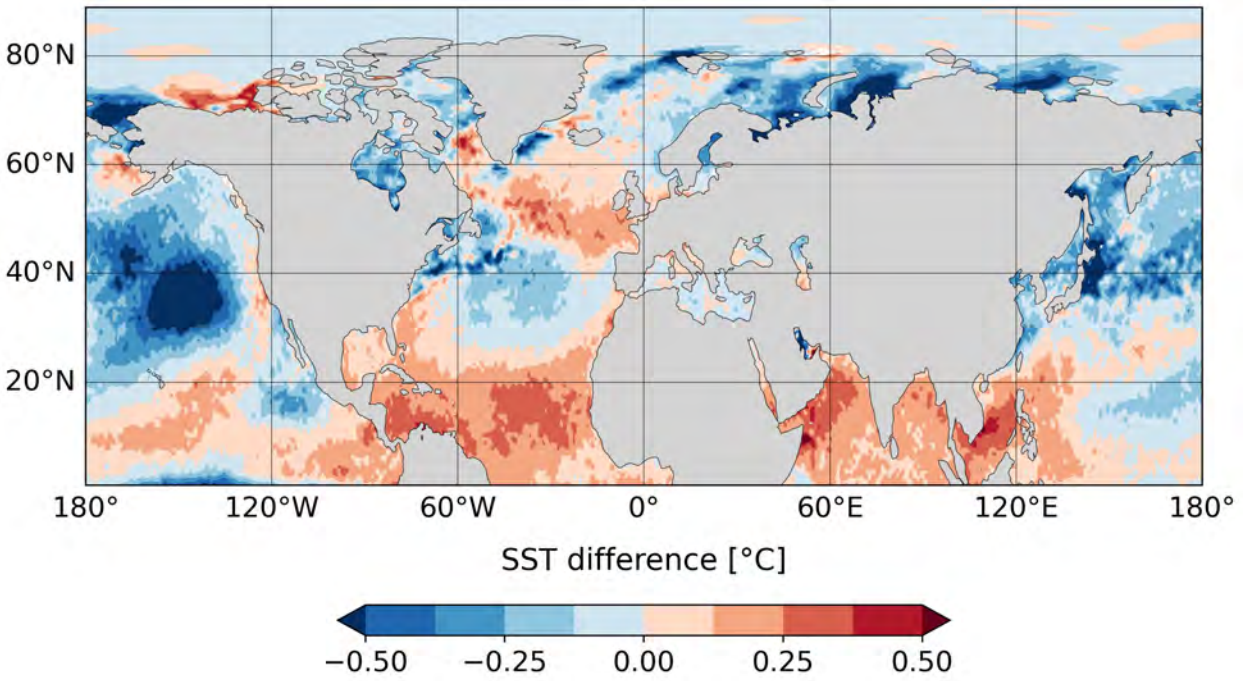

Figure 28: Composites of SST during the 13 La Niña summers minus SST during the total period (1959-2023) for the Northern Hemisphere.

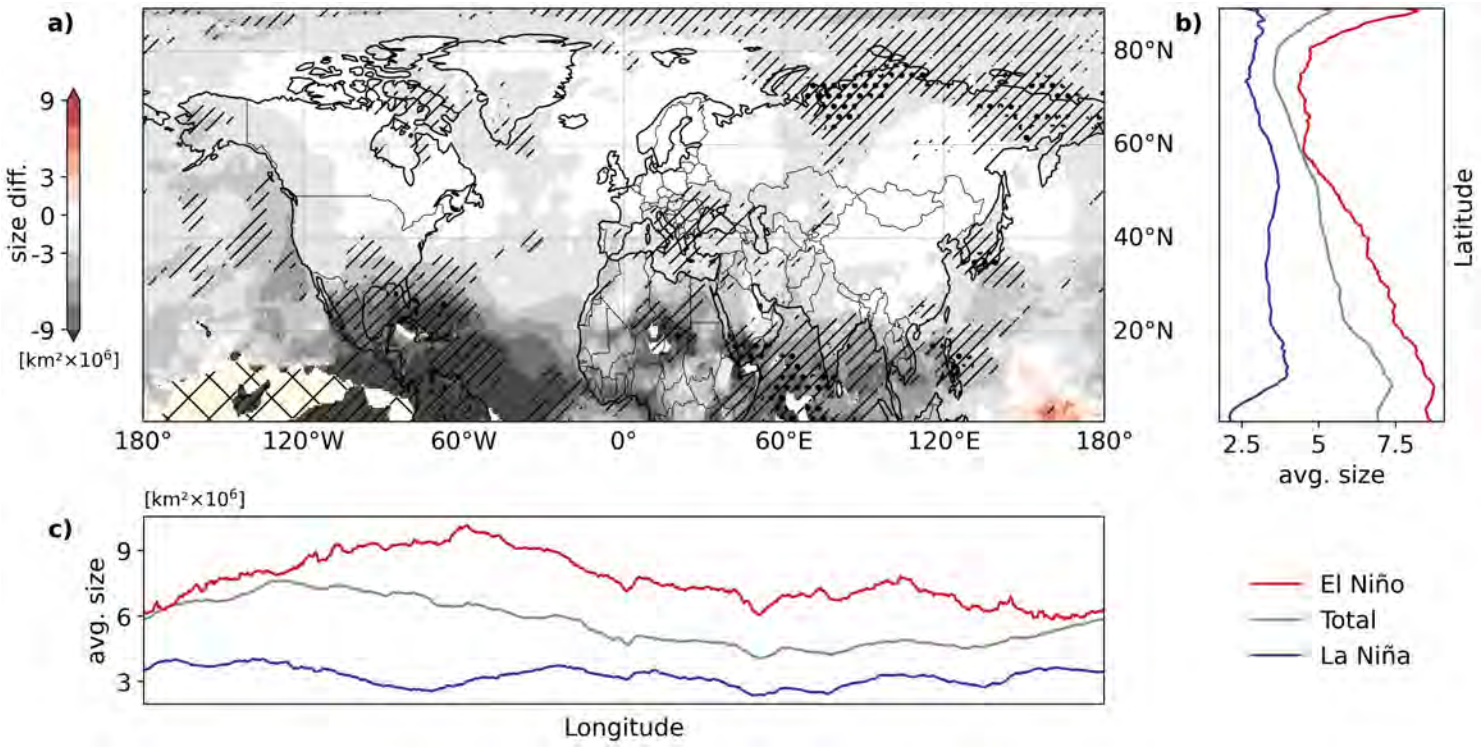

Figure 29: **a)** Composites of heatwave average size during the 13 La Niña summers minus heatwave average size during the total period (1959-2023) for the Northern Hemisphere. Hatching shows where values are in the 5% lower or 5% higher range based on their ranking. Dots indicate areas statistically significant at the 10% level. **b)** Mean average size with latitude during El Niño conditions (in red), La Niña conditions (in blue), and during the total period (in grey). **c)** same as b) but for longitude.

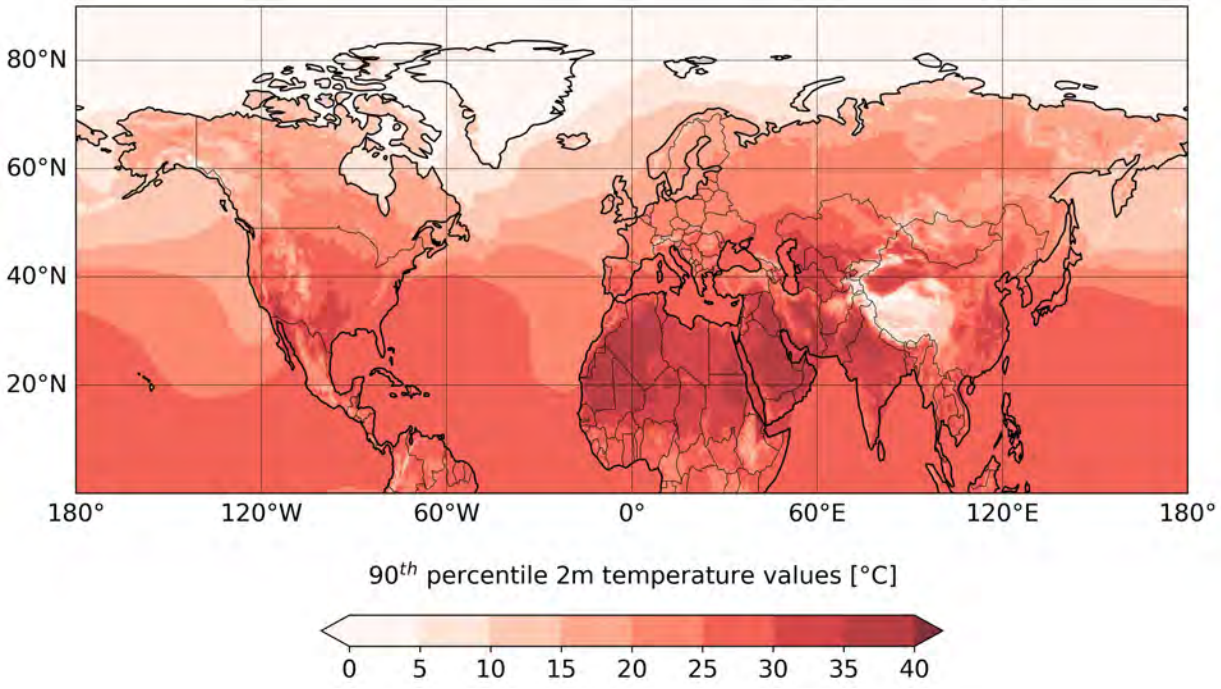

Figure 30: Local 90^{th} percentile based on the daily mean temperature field.

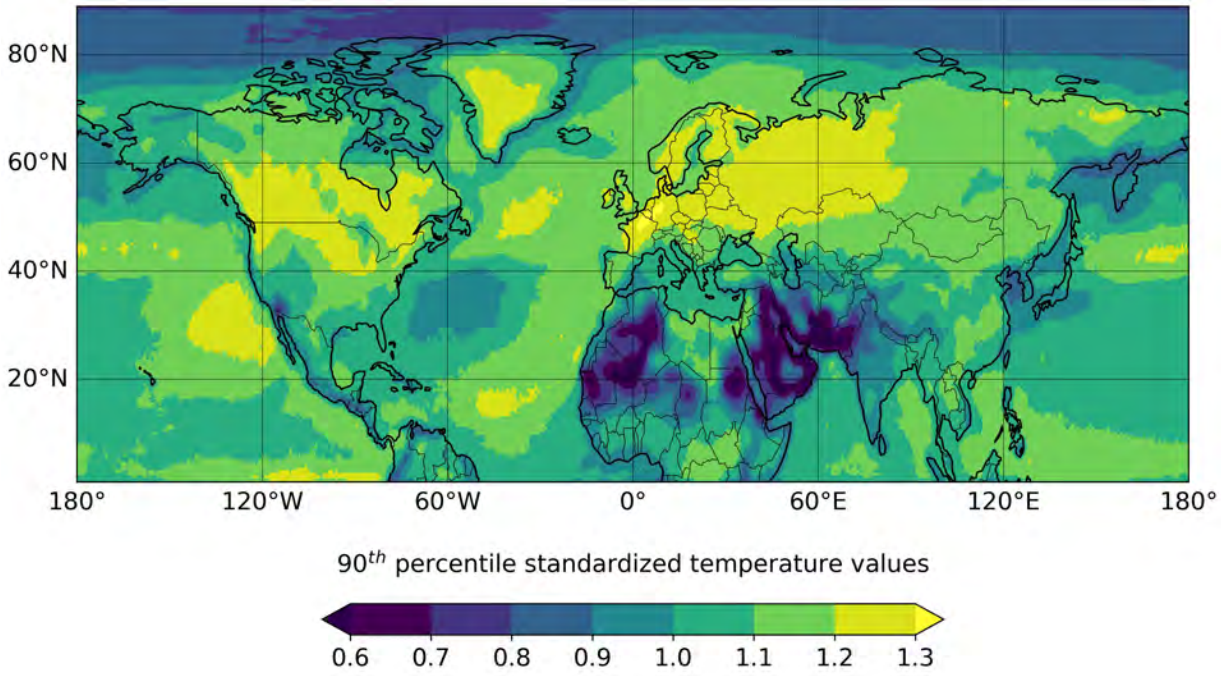

Figure 31: Local 90^{th} percentile based on the standardized temperature anomaly field used with ConTrack.

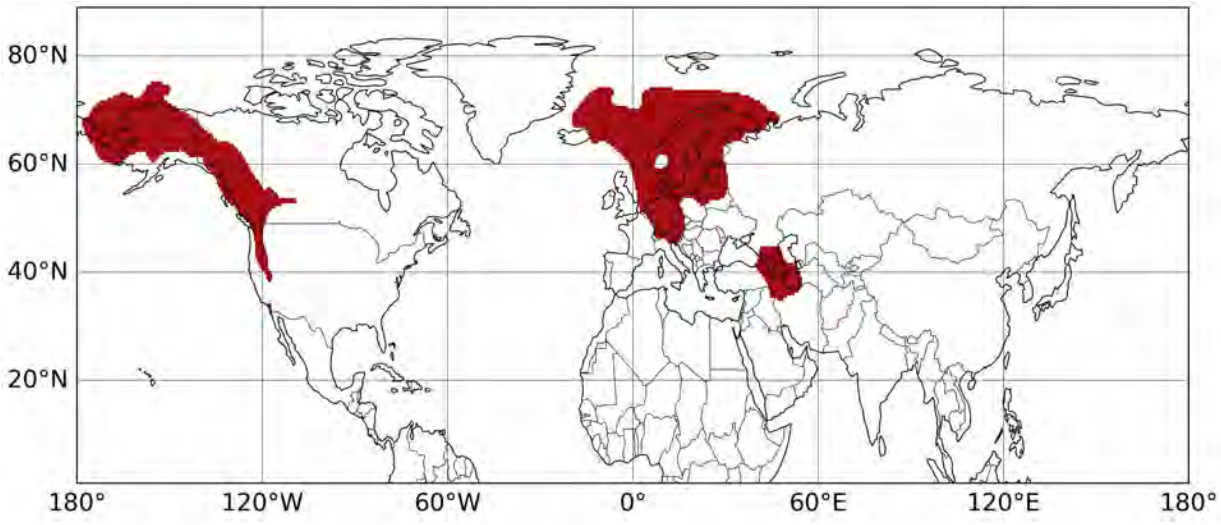

Figure 32: Individual contour (in red) identified by ConTrack on 30.07.2018.

References

Aboelkhair, H., Mohamed, B., Morsy, M., and Nagy, H. (2023). Co-occurrence of atmospheric and oceanic heatwaves in the eastern mediterranean over the last four decades. *Remote Sensing*, 15(7).

Ansah, E. O. and Walsh, O. S. (2021). Impact of 2021 drought in the pacific northwest. *Crops & Soils*, 54(6):46–49.

Beobide-Arsuaga, G., Düsterhus, A., Müller, W., Barnes, E., and Baehr, J. (2023). Spring regional sea surface temperatures as a precursor of european summer heatwaves. *Geophysical Research Letters*, 50.

Berggren, R., Bolin, B., and Rossby, C.-G. (1949). An aerological study of zonal motion, its perturbations and break-down. *Tellus*, 1(2):14–37.

Bieli, M., Pfahl, S., and Wernli, H. (2015). A lagrangian investigation of hot and cold temperature extremes in europe. *Quarterly Journal of the Royal Meteorological Society*, 141(686):98–108.

Borchers Arriagada, N., Bowman, D. M. J. S., Palmer, A. J., and Johnston, F. H. (2020). *Climate Change, Wildfires, Heatwaves and Health Impacts in Australia*, pages 99–116. Springer International Publishing, Cham.

Brás, T. A., Seixas, J., Carvalhais, N., and Jägermeyr, J. (2021). Severity of drought and heatwave crop losses tripled over the last five decades in europe. *Environmental Research Letters*, 16(6):065012.

Brönnimann, S. (2007). Impact of el niño–southern oscillation on european climate. *Reviews of Geophysics*, 45(3).

Böhnisch, A., Felsche, E., and Ludwig, R. (2023). European heatwave tracks: Using causal discovery to detect recurring pathways in a single-regional climate model large ensemble. *Environmental Research Letters*, 18.

Chakraborty, D., Sehgal, V., Dhakar, R., Ray, M., and Das, D. K. (2019). Spatio-temporal trend in heat waves over india and its impact assessment on wheat crop. *Theoretical and Applied Climatology*, 138.

Chan, P., Catto, J., and Collins, M. (2022). Heatwave–blocking relation change likely dominates over decrease in blocking frequency under global warming. *npj Climate and Atmospheric Science*, 5:68.

Chou, C., Tu, J.-Y., and Yu, J.-Y. (2003). Interannual variability of the western north pacific summer monsoon: Differences between enso and non-enso years. *Journal of Climate*, 16:2275–2287.

Darryn McEvoy, I. A. and Mullett, J. (2012). The impact of the 2009 heat wave on melbourne's critical infrastructure. *Local Environment*, 17(8):783–796.

Davey, M., Brookshaw, A., and Ineson, S. (2014). The probability of the impact of enso on precipitation and near-surface temperature. *Climate Risk Management*, 1:5–24.

DiLiberto, T., Becker, E., Johnson, N., L'Heureux, M., and Lindsey, R. (2014). The walker circulation: Enso's atmospheric buddy. `https://www.climate.gov/news-features/blogs/enso/walker-circulation-ensos-atmospheric-buddy`. Last Accessed: 23.05.2024.

Dong, B., Sutton, R., Woollings, T., and Hodges, K. (2013). Variability of the north atlantic summer storm track: Mechanisms and impacts on european climate. *Environmental Research Letters*, 8:4037–.

Feudale, L. and Shukla, J. (2010). Influence of sea surface temperature on the european heat wave of 2003 summer. part i: An observational study. *Climate Dynamics*, 36:1691–1703.

Fischer, E. and Schär, C. (2010). Consistent geographical patterns of changes in high-impact european heatwaves. *Nat Geosci*, 3.

Fonseca, R., Francis, D., Nelli, N., and Thota, M. (2022). Climatology of the heat low and the intertropical discontinuity in the arabian peninsula. *International Journal of Climatology*, 42(2):1092–1117.

Fouillet, A., Rey, G., Laurent, F., Pavillon, G., Bellec, S., Guihenneuc-Jouyaux, C., Clavel, J., Jougla, E., and Hémon, D. (2006). Excess mortality related to the august 2003 heat wave in france. *International archives of occupational and environmental health*, 80:16–24.

Fraga, H., Molitor, D., Leolini, L., and Santos, J. A. (2020). What is the impact of heatwaves on european viticulture? a modelling assessment. *Applied Sciences*, 10(9).

García-León, D., Casanueva, A., Standardi, G., Burgstall, A., Flouris, A., and Nybo, L. (2021). Current and projected regional economic impacts of heatwaves in europe. *Nature Communications*, 12.

Grotjahn, R., Black, R., Leung, L., Wehner, M., Barlow, M., Bosilovich, M., Gershunov, A., Gutowski, W., Gyakum, J., Katz, R., Lee, Y.-Y., Lim, Y.-K., and Prabhat, M. (2015). North american extreme temperature events and related large scale meteorological patterns: Statistical methods, dynamics, modeling, and trends. *Climate Dynamics*, In press.

Hartmann, K., Krois, J., and Rudolph, A. (2023). Statistics and geodata analysis using r (soga-r). *Department of Earth Sciences, Freie Universitaet Berlin.*

Hegedűs, D., Ballinger, A. P., and Hegerl, G. C. (2024). Observed links between heatwaves and wildfires across northern high latitudes. *Environmental Research Letters*, 19(3):034041.

Hersbach, H., Bell, B., Berrisford, P., Hirahara, S., Horányi, A., Muñoz Sabater, J., Nicolas, J., Peubey, C., Radu, R., Schepers, D., Simmons, A., Soci, C., Abdalla, S., Abellan, X., Balsamo, G., Bechtold, P., Biavati, G., Bidlot, J., Bonavita, M., and Thépaut, J.-N. (2020). The era5 global reanalysis. *Quarterly Journal of the Royal Meteorological Society.*

Hoegh-Guldberg, O., Jacob, D., Taylor, M., Bindi, M., Brown, S., Camilloni, I., Diedhiou, A., Djalante, R., Ebi, K., Engelbrecht, F., Guiot, J., Hijioka, Y., Mehrotra, S., Payne, A., Seneviratne, S., Thomas, A., Warren, R., and Zhou, G. (2018). Impacts of 1.5ºc global warming on natural and human systems. in:. *Global Warming of 1.5°C. An IPCC Special Report on the impacts of global warming of 1.5°C above pre-industrial levels and related global greenhouse gas emission pathways, in the context of strengthening the global response to the threat of climate change, sustainable development, and efforts to eradicate poverty.*, [Masson-Delmotte, V., P. Zhai, H.-O. Pörtner, D. Roberts, J. Skea, P.R. Shukla, A. Pirani, W. Moufouma-Okia, C. Péan, R. Pidcock, S. Connors, J.B.R. Matthews, Y. Chen, X. Zhou, M.I.Gomis, E. Lonnoy, T.Maycock, M.Tignor, and T. Waterfield (eds.)]. In Press.

Jiménez-Esteve, B. and Domeisen, D. I. (2022). The role of atmospheric dynamics and large-scale topography in driving heatwaves. *Quarterly Journal of the Royal Meteorological Society*, 148(746):2344–2367.

Kaderli, S. (2023). WaveBreaking - Detection, Classification and Tracking of Rossby Wave Breaking. GitHub, `https://github.com/skaderli/WaveBreaking`.

Ke, X., Wu, D., Rice, J., Kintner-Meyer, M., and Lu, N. (2016). Quantifying impacts of heat waves on power grid operation. *Applied Energy*, 183:504–512.

Keellings, D., Bunting, E., and Engström, J. (2018). Spatiotemporal changes in the size and shape of heat waves over north america. *Climatic Change*, 147.

Kenyon, J. and Hegerl, G. (2008). Influence of modes of climate variability on global temperature extremes. *Journal of Climate*, 21.

Laurila, T. K., Gregow, H., Cornér, J., and Sinclair, V. A. (2021). Characteristics of extratropical cyclones and precursors to windstorms in northern europe. *Weather and Climate Dynamics*, 2(4):1111–1130.

Lavaysse, C., Flamant, C., Janicot, S., Parker, D., Lafore, J.-P., Sultan, B., and Pelon, J. (2009). Seasonal evolution of the west african heat low: A climatological perspective. *Climate Dynamics*, 33:313–330.

Li, C., Lu, R., and Dong, B. (2013). Predictability of the western north pacific summer climate associated with different enso phases by ensembles multi-model seasonal forecasts. *Climate Dynamics*, 43.

Lin, L., Chen, C., and Luo , M. (2018). Impacts of el niño southern oscillation on heat waves in the indochina peninsula. *Atmospheric Science Letters*, 19.

Lorenz, R., Jaeger, E., and Seneviratne, S. (2010). Persistence of heat waves and its link to soil moisture memory. *Geophysical Research Letters - GEOPHYS RES LETT*, 37.

Luo, M. and Lau, N.-C. (2019). Amplifying effect of enso on heat waves in china. *Climate Dynamics*, 52.

Luo, M. and Lau, N.-C. (2020). Summer heat extremes in northern continents linked to developing enso events. *Environmental Research Letters*, 15(7):074042.

Luo, M., Lau, N.-C., Liu, Z., Wu, S., and Wang, X. (2022). An observational investigation of spatiotemporally contiguous heatwaves in china from a 3d perspective. *Geophysical Research Letters*, 49(6):e2022GL097714. e2022GL097714 2022GL097714.

Luo, M., Wu, S., Lau, G. N.-C., Pei, T., Liu, Z., Wang, X., Ning, G., Chan, T. O., Yang, Y., and Zhang, W. (2024). Anthropogenic forcing has increased the risk of longer-traveling and slower-moving large contiguous heatwaves. *Science Advances*, 10(13):eadl1598.

Lyon, B., Barnston, A. G., Coffel, E., and Horton, R. M. (2019). Projected increase in the spatial extent of contiguous us summer heat waves and associated attributes. *Environmental Research Letters*, 14(11):114029.

Marx, W., Haunschild, R., and Bornmann, L. (2021). Heat waves: a hot topic in climate change research. *Theoretical and Applied Climatology*, 146.

McKinnon, K. A. and Simpson, I. R. (2022). How unexpected was the 2021 pacific northwest heatwave? *Geophysical Research Letters*, 49(18):e2022GL100380. e2022GL100380 2022GL100380.

Meehl, G. A. and Tebaldi, C. (2004). More intense, more frequent, and longer lasting heat waves in the 21st century. *Science*, 305(5686):994–997.

Mokhov, I., Chernokulsky, A., and Osipov, A. (2020). Atmospheric centers of action in the northern and southern hemispheres: Features and variability. *Russian Meteorology and Hydrology*, 45:749–761.

Neal, E., Huang, C., and Nakamura, N. (2022). The 2021 pacific northwest heat wave and associated blocking: Meteorology and the role of an upstream cyclone as a diabatic source of wave activity. *Geophysical Research Letters*, 49.

NOAA (2024). Oceanic niño index (oni). `https://origin.cpc.ncep.noaa.gov/products/analysis_monitoring/ensostuff/ONI_v5.php`. Last Accessed: 03.04.2024.

Orlov, A., Sillmann, J., Aaheim, A., Aunan, K., and Bruin, K. (2019). Economic losses of heat-induced reductions in outdoor worker productivity: a case study of europe. *Economics of Disasters and Climate Change*, 3.

Ouyang, X., Lao, W., and Lao, M. (2023). Change of probability density distributions of summer temperatures in different climate zones. *Frontiers of Earth Science*.

Overland, J. E. (2021). Causes of the record-breaking pacific northwest heatwave, late june 2021. *Atmosphere*, 12(11).

Pai, D., Nair, S., and IMD, M. (2022). Impact of el-niño-southern oscillation (enso) on extreme temperature events over india. *MAUSAM*, 73:597–606.

Parente, J., Pereira, M., Amraoui, M., and Fischer, E. (2018). Heat waves in portugal: Current regime, changes in future climate and impacts on extreme wildfires. *Science of The Total Environment*, 631-632:534–549.

Perkins, S. E. (2015). A review on the scientific understanding of heatwaves—their measurement, driving mechanisms, and changes at the global scale. *Atmospheric Research*, 164-165:242–267.

Perkins, S. E. and Alexander, L. V. (2013). On the measurement of heat waves. *Journal of Climate*, 26(13):4500 – 4517.

Perkins-Kirkpatrick, S. and Lewis, S. (2020). Increasing trends in regional heatwaves. *Nature Communications*, 11:3357.

Pfahl, S. (2014). Characterising the relationship between weather extremes in europe and synoptic circulation features. *Natural hazards and earth system sciences*, 2.

Pfahl, S. and Wernli, H. (2012). Quantifying the relevance of atmospheric blocking for co-located temperature extremes in the northern hemisphere on (sub-)daily time scales. *Geophysical Research Letters*, 39(12).

Philip, S., Kew, S., Van Oldenborgh, G. J., Anslow, F., Seneviratne, S., Vautard, R., Coumou, D., Ebi, K., Arrighi, J., Singh, R., Aalst, M., Pereira Marghidan, C., Wehner, M., Yang, W., Li, S., Schumacher, D., Hauser, M., Bonnet, R., Luu, L., and Otto, F. (2021). Rapid attribution analysis of the extraordinary heatwave on the pacific coast of the us and canada june 2021.

Qian, Y., Hsu, P.-C., Yuan, J., Zhu, Z., Wang, H., and Duan, M. (2022). Effects of subseasonal variation in the east asian monsoon system on the summertime heat wave in western north america in 2021. *Geophysical Research Letters*, 49(8):e2021GL097659.

Reddy, P. J., Perkins-Kirkpatrick, S. E., and Sharples, J. J. (2021). Interactive influence of enso and iod on contiguous heatwaves in australia. *Environmental Research Letters*, 17(1):014004.

Rex, D. F. (1950). Blocking action in the middle troposphere and its effect upon regional climate. *Tellus*, 2(4):275–301.

Robine, J.-M., Cheung, S. L. K., Roy, S. L., Oyen, H. V., Griffiths, C., Michel, J.-P., and Herrmann, F. R. (2008). Death toll exceeded 70,000 in Europe during the summer of 2003. *Comptes Rendus. Biologies*, 331(2):171–178.

Rogers, C. D. W., Gallant, A. J. E., and Tapper, N. J. (2019). Is the urban heat island exacerbated during heatwaves in southern Australian cities? *Theoretical and Applied Climatology*, 137(1-2):441–457.

Rogers, C. D. W., Kornhuber, K., Perkins-Kirkpatrick, S. E., Loikith, P. C., and Singh, D. (2022). Sixfold increase in historical northern hemisphere concurrent large heatwaves driven by warming and changing atmospheric circulations. *Journal of Climate*, 35(3):1063 – 1078.

Röthlisberger, M. and Papritz, L. (2023). Quantifying the physical processes leading to atmospheric hot extremes at a global scale. *Nature Geoscience*, 16:1–7.

Scaife, A., Comer, R., Dunstone, N., Fereday, D., Folland, C., Good, E., Gordon, M., Hermanson, L., Ineson, S., Karpechko, A., Knight, J., MacLachlan, C., Maidens, A., Peterson, K., Smith, D., Slingo, J., and Walker, B. (2017). Predictability of european winter 2015/2016: Winter predictability. *Atmospheric Science Letters*, 18.

Schneider, T., Bischoff, T., and Plotka, H. (2014). Physics of changes in synoptic midlatitude temperature variability. *Journal of Climate*, 28.

Schumacher, D. L., Hauser, M., and Seneviratne, S. I. (2022). Drivers and mechanisms of the 2021 pacific northwest heatwave. *Earth's Future*, 10(12):e2022EF002967. e2022EF002967 2022EF002967.

Schwierz, C., Croci-Maspoli, M., and Davies, H. C. (2004). Perspicacious indicators of atmospheric blocking. *Geophysical Research Letters*, 31(6).

Schär, C., Vidale, P., Lüthi, D., Frei, C., Häberli, C., Liniger, M., and Appenzeller, C. (2004). 2004: The role of increasing temperature variability in european summer heatwaves. *Nature*, 427:332–6.

Seneviratne, S. I., Zhang, X., Adnan, M., Badi, W., Dereczynski, C., Di Luca, A., Ghosh, S., Iskandar, I., Kossin, J., Lewis, S., Otto, F., Pinto, I., Satoh, M., Vicente-Serrano, S. M., Wehner, M., and Zhou, B. (2021). Weather and climate extreme events in a changing climate. *Cambridge University Press, Cambridge, United Kingdom and New York, NY, USA*, page 1513–1766.

Steinfeld, D. (2020). ConTrack - Contour Tracking. GitHub, `https://github.com/steidani/ConTrack`.

Steinfeld, D., Boettcher, M., Forbes, R., and Pfahl, S. (2020). The sensitivity of atmospheric blocking to upstream latent heating – numerical experiments. *Weather and Climate Dynamics*, 1(2):405–426.

Steinfeld, D., Sprenger, M., Beyerle, U., and Pfahl, S. (2022). Response of moist and dry processes in atmospheric blocking to climate change. *Environmental Research Letters*, 17(8):084020.

Steinfled, D. and Pfahl, S. (2019). The role of latent heating in atmospheric blocking dynamics: a global climatology. *Climate Dynamics*, 53:6159–6180.

Stocker, T., Fischer, H., Joos, F., Leuenberger, M., Frölicher, T., and Raible, C. (2020). Introduction to climate and environmental physics. *Lecture Notes, Autumn Semester 2020, University of Bern*.

Stéfanon, M., D'Andrea, F., and Drobinski, P. (2012). Heatwave classification over europe and the mediterranean region. *Environmental Research Letters*, 7:014023.

Suarez, M. J. and Schopf, P. S. (1988). A delayed action oscillator for enso. *Journal of Atmospheric Sciences*, 45(21):3283 – 3287.

Tamarin-Brodsky, T., Hodges, K., Hoskins, B., and Shepherd, T. (2020). Changes in northern hemisphere temperature variability shaped by regional warming patterns. *Nature Geoscience*, 13:1–8.

Thompson, R., Hornigold, R., Page, L., and Waite, T. (2018). Associations between high ambient temperatures and heat waves with mental health outcomes: a systematic review. *Public Health*, 161:171–191. Special issue on Health and high temperatures.

Thompson, V., Kennedy-Asser, A. T., Vosper, E., Lo, Y. T. E., Huntingford, C., Andrews, O., Collins, M., Hegerl, G. C., and Mitchell, D. (2022). The 2021 western north america heat wave among the most extreme events ever recorded globally. *Science Advances*, 8(18):eabm6860.

Trenberth, K. E., Caron, J. M., Stepaniak, D. P., and Worley, S. (2002). Evolution of el niño–southern oscillation and global atmospheric surface temperatures. *Journal of Geophysical Research: Atmospheres*, 107(D8):AAC 5–1–AAC 5–17.

Trepanier, J. (2020). North atlantic hurricane winds in warmer than normal seas. *Atmosphere*, 11:293.

Tuel, A. and Martius, O. (2024). Persistent warm and cold spells in the northern hemisphere extratropics: regionalisation, synoptic-scale dynamics and temperature budget. *Weather and Climate Dynamics*, 5(1):263–292.

Tuel, A., Steinfeld, D., Ali, S. M., Sprenger, M., and Martius, O. (2022). Large-scale drivers of persistent extreme weather during early summer 2021 in europe. *Geophysical Research Letters*, 49.

Vicedo-Cabrera, A., Scovronick, N., Sera, F., Royé, D., Schneider, R., Tobias, A., Åström, C., Guo, Y., Honda, Y., Hondula, D., Abrutsky, R., Tong, S., Sousa, M., Coelho, Z., Saldiva, P., Lavigne, E., Correa, P., Valdes Ortega, N., Kan, H., and Holobaca, I. (2021). The burden of heat-related mortality attributable to recent human-induced climate change. *Nature Climate Change*, 182.

Vogel, M. M., Zscheischler, J., Fischer, E. M., and Seneviratne, S. I. (2020). Development of future heatwaves for different hazard thresholds. *Journal of Geophysical Research: Atmospheres*, 125(9):e2019JD032070.

Vogt, L., Burger, F. A., Griffies, S. M., and Frölicher, T. L. (2022). Local drivers of marine heatwaves: A global analysis with an earth system model. *Frontiers in Climate*, 4.

Westerling, A. L., Hidalgo, H. G., Cayan, D. R., and Swetnam, T. W. (2006). Warming and earlier spring increase western u.s. forest wildfire activity. *Science*, 313(5789):940–943.

White, R., Anderson, S., Booth, J., Braich, G., Draeger, C., Fei, C., Harley, C., Henderson, S., Jakob, M., Lau, C.-A., Admasu, L. M., Narinesingh, V., Rodell, C., Roocroft, E.,

Weinberger, K., and West, G. (2023). The unprecedented pacific northwest heat- wave of june 2021. *Nature Communications*, 14.

Wilks, D. S. (2016). "the stippling shows statistically significant grid points": How research results are routinely overstated and overinterpreted, and what to do about it. *Bulletin of the American Meteorological Society*, 97(12):2263 – 2273.

Woollings, T., Barriopedro, D., Methven, J., Son, S.-W., Martius, O., Harvey, B., Sillmann, J., Lupo, A., and Seneviratne, S. (2018). Blocking and its response to climate change. *Current Climate Change Reports*, 4:1–14.

Wu, S., Luo, M., Liu, Z., Wang, X., Huang, Z., and Li, X. (2024). Longer- and slower-moving contiguous heatwaves linked to el niño. *Geophysical Research Letters*, 51(11):e2024GL109067. e2024GL109067 2024GL109067.

Xia, Y., Li, Y., Guan, D., Tinoco, D. M., Xia, J., Yan, Z., Yang, J., Liu, Q., and Huo, H. (2018). Assessment of the economic impacts of heat waves: A case study of nanjing, china. *Journal of Cleaner Production*, 171:811–819.

Zampieri, M., D'Andrea, F., Vautard, R., Ciais, P., de NOBLET, N., and Yiou, P. (2009). Hot european summers and the role of soil moisture in the propagation of mediterranean drought. *Journal of Climate*, 22:4747–4758.

Zschenderlein, P., Fink, A., Pfahl, S., and Wernli, H. (2019). Processes determining heat waves across different european climates. *Quarterly Journal of the Royal Meteorological Society*, 145:2973–2989.

Additional Tools

Tool	Application	Affected part of the work
Grammarly, 2024, `https://www.grammarly.com/`	Text correction (e.g., grammar, spelling)	Entire text
ChatGPT (OpenAI), 2024, `https://openai.com/chatgpt/`	Text editing, correction, and refinement	Entire text

Acknowledgements

I would like to thank my two advisors, Edgar Dolores-Tesillos and Duncan Pappert, for their valuable time, patience, and constant support throughout this thesis. I also want to thank my supervisor, Olivia Romppainen-Martius, for her insightful suggestions and feedback.

I would also like to thank all my friends for making it such a great experience. Lastly, I want to thank my family for their support and encouragement in allowing me to pursue this degree and follow my dreams.

Declaration of consent

on the basis of Article 30 of the RSL Phil.-nat. 18

Name/First Name: Hartmann/ Nicolas

Registration Number: 18-326-058

Study program: Msc in Climate Sciences

Bachelor ☐ Master ☑ Dissertation ☐

Title of the thesis: Tracking Heatwaves in the Northern Hemisphere

Supervisor: Prof. Dr. Olivia Romppainen-Martius

I declare herewith that this thesis is my own work and that I have not used any sources other than those stated. I have indicated the adoption of quotations as well as thoughts taken from other authors as such in the thesis. I am aware that the Senate pursuant to Article 36 paragraph 1 litera r of the University Act of 5 September, 1996 is authorized to revoke the title awarded on the basis of this thesis.

For the purposes of evaluation and verification of compliance with the declaration of originality and the regulations governing plagiarism, I hereby grant the University of Bern the right to process my personal data and to perform the acts of use this requires, in particular, to reproduce the written thesis and to store it permanently in a database, and to use said database, or to make said database available, to enable comparison with future theses submitted by others.

Genève/ 17.06.2024

Place/Date

Signature